Rotation of a Slender Rod Injected into a Cylindrical Constraint

by

Connor Gordon Mulcahy

B.M.E, University of Minnesota (2013)

Submitted to the Department of Mechanical Engineering
in partial fulfillment of the requirements for the degree of

Master of Science in Mechanical Engineering

at the

MASSACHUSETTS INSTITUTE OF TECHNOLOGY

February 2016

Signature redacted

Author .....
Department of Mechanical Engineering
January 19, 2015

Signature redacted

Certified by .....
Pedro M. Reis
Associate Professor of Mechanical Engineering and Civil and Environmental Engineering
Thesis Supervisor

Signature redacted

Accepted by .....
Rohan Abeyaratne
Quentin Berg Professor of Mechanics
Chairman, Committee on Graduate Students

Rotation of a Slender Rod Injected into a Cylindrical Constraint

by

Connor Gordon Mulcahy

Submitted to the Department of Mechanical Engineering
on January 19, 2015, in partial fulfillment of the
requirements for the degree of
Master of Science in Mechanical Engineering

Abstract

We investigate the buckling of a slender elastic rod injected into a cylindrical constraint while undergoing axial rotation. Particular focus is given to extension of the helical buckling length. This problem is of particular application to coiled tubing operations in the oil and gas industry where helical buckling and eventual lockup occur, thereby preventing complete access to horizontal oil wells. Our approach focuses on using desktop experiments to perform a precise exploration of the parameters affecting buckling. We examine two separate modes of axial rotation: continuous rotation and oscillatory rotation. In each case, we demonstrate potential for significant increases in helical buckling length by a factor of as much as 5 within the parameter space studied and develop an understanding of the underlying mechanisms at play. In the case of continuous rotation, we compare our experimental results to theoretical predictions motivated by this work. The extensions in helical buckling length observed here suggest significant application to the problem of helical buckling in coiled tubing operations.

Thesis Supervisor: Pedro M. Reis
Title: Associate Professor of Mechanical Engineering and Civil and Environmental Engineering

Acknowledgments

As I conclude this thesis, there are several of people to whom I would like to express my gratitude. First, I would like to thank Professor Reis for his supervision and advice throughout this work. Additionally, none of this would have been possible without the funding and support of everyone at Schlumberger-Doll Research.

On a more personal note, I would like to thank those in my life who supported me throughout my graduate work: the esteemed post-docs of the EGS lab, Francisco and Joel, who were always willing to provide advice, wisdom, and, most importantly, coffee; and all of my friends at MIT who made the past two years a truly wonderful experience.

Lastly, thank you to my parents for their constant support throughout my college career.

Contents

Chapter 1

Introduction

1.1 Motivation

Developments in directional drilling in the oil and gas industry have promoted the construction of horizontal wellbores [1]. These wellbores consist of a vertical section extending downward, followed by a curved section in which the wellbore transitions into a horizontal section that extends into the oil-producing area at a small (less than 10 degrees) angle to the horizontal. This horizontal section can extend to lengths as far as 11.7 km [2]. While this type of wellbore offers substantial production possibilities for oilfield exploration [3, 4], it also presents significant technical challenges.

Once a wellbore has been drilled, various service procedures become essential for efficient operation, including cleaning, data acquisition, and recovering of downhole debris [5, 6]. These tasks are typically accomplished using coiled tubing; a continuous length of steel tubing initially coiled around a large reel, this tubing is injected into the wellbore from the surface. This process is complicated in horizontal wellbores by the gravity-induced frictional contact between the tubing and the borehole in its horizontal section. As increasing lengths of coiled tubing are injected, the contact area between the tubing and borehole increases, causing escalation of frictional compressive forces [7]. When these forces reach a critical level, buckling and eventual lockup of the coiled tubing occurs, barring further injection [8]. This phenomenon results in the inability of coiled tubing to access the entire length of many existing horizontal

wellbores.

Previous studies have explored means of extending the reach of coiled tubing into a horizontal wellbore by focusing on attempts to improve system parameters to delay buckling, such as optimizing the diameter of the coiled tubing [9] or decreasing friction between the coiled tubing and borehole using lubricants [10]. Mechanical means of reach extension have also been considered, including use of downhole tractors [11] and distributed vibration of the coiled tubing [12]. Axial rotation has been shown to reduce the overall axial forces on the constrained rod, thus delaying the onset of buckling [13]. However, these past investigations were primarily focused on coiled tubing drilling operations and were conducted at field scale. A more systematic experimental and theoretical investigation into the feasibility of axial rotation to improve reach in coiled tubing would be of significant benefit to the oil and gas industry.

In this thesis, we present the results of precision desktop experiments that we developed to investigate the potential of using axial rotation to improve reach extension in coiled tubing operations.

1.2 Previous Work

Buckling of a constrained rod is not a problem unique to coiled tubing. Similar buckling phenomena have been investigated in a variety of fields and scales, including catheters passed through blood vessels [14], silicon nanorods confined within a channel [15], and DNA folded inside a viral capsule [16]. Previous academic investigations into cylindrically constrained buckling have focused on two separate boundary conditions, the axial compression of a cylindrically constrained rod [17, 18] and injection of a rod into a horizontal cylinder [19].

1.2.1 Axial Compression of a Cylindrically Constrained Rod

The study of axial compression of a cylindrically constrained rod has been principally motivated by drilling in the oil and gas industry. During this process, the drill string,

consisting of several long segments of pipe screwed together, is clamped both at the top of the wellbore at the drill rig and at the distal end by contact between the drill head and the material being penetrated. The nature of drilling operations requires significant axial compression of the drill string to allow for advancement. When this compressive force reaches a critical value, buckling of the drill string ensues.

Academic inquiries have generally focused on the representative system of a length of rod under axial compression within a cylindrical constraint as shown schematically in Figure 1-1. As the rod is compressed, it initially buckles into a sinusoidal mode with wavelength λ, followed by a helical buckling mode with pitch p.

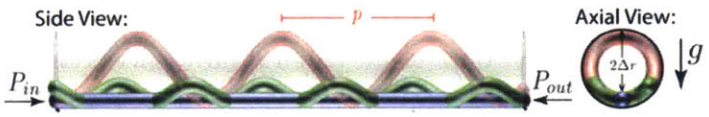

Figure 1-1: Schematic diagram showing axial compression of a length of rod within a horizontal cylinder. As the rod is compressed, it buckles from an initially straight configuration (blue), to a sinusoidal buckling mode (green) with wavelength λ, and finally to a helical mode (red) with pitch p. Figure extracted from [20]

The first investigations into this buckling behavior were conducted by Lubinski et al. [17, 18], who derived an initial buckling mode for the case of a rod within a vertical cylinder compressed past the point of sinusoidal buckling. Subsequently, Paslay and Bogey [21] employed energy arguments to derive expressions for the critical buckling load for sinusoidal buckling, F_{cr}^{s}, of a rod within a frictionless inclined cylinder, in which there is no contact loss between rod and constraint. Later, research by Dawson and Paslay [22] derived expressions for the wavelength of this sinusoidal rod buckling, λ_s, in an inclined cylindrical constraint.

Helical buckling of a rod constrained in a vertical cylinder was also first described in the early investigations of Lubinski et al. [18]. This work resulted in a prediction for the relationship between the axial load on the rod and the helical buckling pitch. Subsequent examination by Chen et al. [23] led to the derivation of the critical force required for the onset of helical buckling of a constrained rod. These predictions of buckling behavior have since been experimentally verified by Miller et al.[20].

1.2.2 Injection of a Rod into a Horizontal Cylinder

In the case of most coiled tubing operations, the boundary conditions are different from those described above. In horizontal oil wellbores, the coiled tubing is clamped at the point of injection, while the distal end is free. The compressive loads exerted on the tubing are primarily due to gravity-driven frictional forces from contact with the borehole.

Academic investigations of the buckling of coiled tubing have focused on the problem of a length of rod injected into a horizontal cylinder. As a rod is injected into a horizontal cylindrical constraint, a compressive axial force builds up due to frictional contact with the constraint. When this axial force reaches a critical level, buckling occurs. Wicks et al. and McCourt et al. [24, 19] have successfully expanded on the above work for a cylindrically constrained rod under axial compression to describe this behavior. During injection, the maximum axial force acting on the rod exists at the injection site. Wicks et al. [19] defined this force by integrating the frictional forces along the entire length of the rod as:

$$F_{inj} = \mu_a w l. \tag{1.1}$$

where l is the total injected length of rod ($s = 0$ at the tip), $w = \rho A g$ is the weight per unit length of the rod (where ρ and A are the density and cross sectional area of the rod respectively and g is the acceleration due to gravity), and μ_a is the coefficient of friction between the rod and the constraint in the axial direction. The rod buckles into a sinusoidal mode when this force reaches a critical value given by Paslay and Bogey [21]:

$$F_{cr}^{s} = 2\left(\frac{EIw}{\Delta r}\right)^{1/2}. \tag{1.2}$$

Here, E and I are the elastic modulus and bending moment of inertia of the rod respectively and Δr is the radial clearance between the rod and the constraint. The wavelength of this sinusoidal buckling mode has been derived by Dawson and

Paslay [22]:

$$\lambda_s = 2\pi \left(\frac{EI\Delta r}{w} \right)^{1/4}. \tag{1.3}$$

There is significant spatial heterogeneity in the buckled configuration of the rod. Sinusoidal buckling initiates at the injection site, while a portion of the rod extending to the free tip remains in the straight unbuckled configuration.

As the rod is injected further, F_{inj} continues to increase, eventually reaching a second critical force predicted by Chen et al. [25]:

$$F_{cr}^{h} = 2\sqrt{2} \left(\frac{EIw}{\Delta r} \right)^{(1/2)}. \tag{1.4}$$

At this point, the rod buckles into a helical mode. The configuration of the rod remains spatially heterogeneous: the helical portion is observed at the injection site (where the compressive axial force is the highest), followed by an intermediate sinusoidal configuration, and finally straightening near the rod tip. Using the fact that $F_a = F_{cr}^{h}$ at this point, from Equations 1.4 and 1.1, Wicks et al. [19] concluded that the length of rod injected at the onset of helical buckling is given by:

$$l_{h,\omega=0} = \frac{2\sqrt{2}}{\mu_a} \left(\frac{EI}{w\Delta r} \right)^{1/2} \tag{1.5}$$

This equation serves as a prediction for the helical buckling length of a rod injected into a horizontal constraint in the absence of axial rotation ($\omega = 0$). In this thesis, we will build on the work of Wicks et al. [19] to expand Equation 1.5 to include the effects of continuous axial rotation of the rod.

Experimental investigations by Miller et al. [12, 20] on the injection of a rod into a horizontal constraint consisted of a length of polymeric rod injected into a borosilicate glass tube. This work demonstrated agreement with the theoretical predictions of Wicks et al. This work also included significant experimental and numeric investigations into the possibility of distributed vibration of the rod as a method of

increasing the helical buckling length.

1.3 Thesis Outline

This thesis is organized as follows. Chapter 2 provides a theoretical background of buckling behavior of a rod injected into a cylindrical constraint. In addition, a novel theory is presented that was developed at Schlumberger-Doll Research to predict the reach extension provided by continuous axial rotation of an injected rod. In Chapter 3, these theoretical predictions of reach extension are validated. An experimental apparatus was fabricated to explore reach extension provided by simultaneous axial rotation and injection of a rod into a cylindrical constraint and to verify several assumptions made in the derivation of the theory. In Chapter 4, we present the results of these investigations into the effects of oscillatory rotation on buckling behavior. Results and conclusions are summarized in Chapter 5 and possible areas for future exploration are proposed.

Chapter 2

Background and Theory

In this chapter, we describe the theoretical framework required for understanding the buckling behavior of a rod injected into a cylindrical constraint while undergoing axial rotary motion. The results of this theoretical analysis will be used to rationalize the experimental results presented in Chapter 3. § 2.1 provides a description of the problem. Next, § 2.2 presents a theory that quantifies the increase in the buckling length of a rod undergoing continuous rotation during injection into a cylindrical constraint.

2.1 Description of the Problem

A schematic diagram of the problem investigated in this thesis is shown in Figure 2-1. A thin elastic rod of radius R is injected into a borosilicate tube of inner diameter D at a speed v. During injection, the rod is subjected to axial rotations at the injection site with speed ω. In the case of continuous rotation as described by the theory derived below, ω is a constant. However, in the case of the experiments reported in this thesis, we also consider the case of oscillitory rotation with a non-constant value of ω. Since this work focuses on increasing the reach of coiled tubing prior to helical buckling, the primary value of interest is the helical buckling length, l_h. When reporting reach extension results, we utilize the normalized helical buckling length, $\bar{l_h} = l_h/l_{h,\omega=0}$, which is simply the helical buckling length normalized by the helical

buckling length of a rod injected into the same constraint in the absence of axial rotation ($\omega = 0$) as predicted by Equation 1.5.

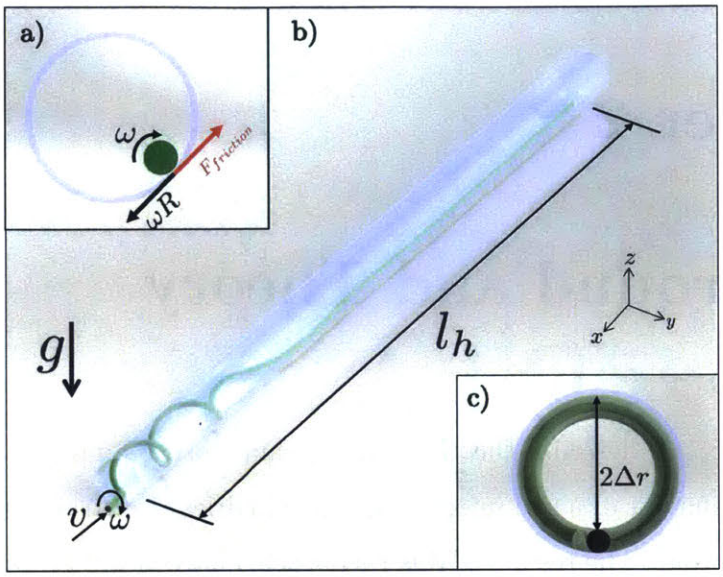

Figure 2-1: Diagram of buckling of a rod injected into a constraint. (a) Vector diagram of transverse forces acting on a rod during axial rotation. (b) Diagram of helical buckling state. For static injection, the axial rotation speed ω is equal to zero. (c) Definition of radial clearance.

2.2 Continuous Rotation

In Chapter 3, we will present a body of experimental work that investigates the buckling behavior of a rod injected into a constraint while undergoing continuous rotation around its axis. In order to apply this work to practical applications such as coiled tubing operations, it is necessary to develop a theoretical understanding of the effects of continuous rotation on buckling length. In § 2.2.1, a basic theory is presented which considers only factors that increase reach with continuous rotation. In § 2.2.2, a more advanced theory is developed, which also considers normal force and twisting factors that tend to decrease reach. Unless otherwise noted, the theory considered in this section is the work of Dr. Tianxiang Su (Schlumberger-Doll Research), which was motivated by the experimental results of the author, and is yet unpublished.

2.2.1 Extended Reach by Rotation: Basic Theory

In the non-rotating case, the velocity of any point along the surface of the rod has only one component, which is axial. The presence of rotation adds a second transverse component that points perpendicularly to the axial component (see Figure 2-1a). The frictional force, $\mathbf{f}$, acting at the contact points between the rod and constraint directly opposes these vectors and is given (per unit length) as:

$$\mathbf{f} = (f_a, f_t) = \left(-\frac{\mu_a N}{\sqrt{1+\alpha^2}}, -\frac{\mu_t \alpha N}{\sqrt{1+\alpha^2}} \right) \tag{2.1}$$

Where N represents the normal force per unit length of the rod, μ_a and μ_t are components of the coefficient of friction between the rod and constraint in the axial and transverse directions, respectively, and α is the velocity ratio. This ratio is a dimensionless parameter selected to describe this system and is given by:

$$\alpha = \frac{\omega R}{v} \tag{2.2}$$

where ω is the rotation speed, R is the radius of the rod, and v is the injection speed. The value of α is assumed to be constant throughout the length of the rod.

An important effect of rod rotation within a cylindrical constraint is that the presence of a transverse velocity component causes the rod to rise up the side of the constraint to an angle given by:

$$\theta_r = \arctan(\mu_t). \tag{2.3}$$

A consequence of this rise is that part of the transverse frictional force now points in the vertical direction, thus decreasing the normal contact force, N, between the rod and the constraint. It can be shown, by considering a force balance of the transverse

forces acting on the rod, that there is a relationship between N and μ_t given by:

$$N = \frac{\rho g A}{\sqrt{1 + \mu_t^2 \alpha^2/(1+\alpha^2)}}. \tag{2.4}$$

From Equation 2.4, it can be seen that an increase in α will result in a decrease of the value of N. By plugging Equation 2.4 into Equation 2.1 and integrating, an expression for the total axial force acting on a point along the arc length of the rod can be obtained:

$$F_a = \int_0^s f_a ds = \frac{\mu_a \rho g A s}{\sqrt{1 + (1+\mu_t^2)\alpha^2}}. \tag{2.5}$$

Note that F_a increases linearly with s. Thus, it will reach a maximum at the farthest point from the rod tip $s = l$, where l is the total injected length (i.e., at the injection point).

In order to use this equation to predict the onset of buckling, it should be noted that buckling occurs when the compressive force in the rod equals a critical force value:

$$F_a = F_{cr}. \tag{2.6}$$

By substituting Equation 2.5 into Equation 2.6, an expression for the critical buckling length, l_h, can be obtained:

$$l_h = \sqrt{1 + (1+\mu_t^2)\alpha^2}\, \frac{F_{cr}}{\mu_a \rho g A}. \tag{2.7}$$

Assuming that the value of F_{cr} is independent of rotation, a normalized measure of buckling length extension, $\bar{l_h}$, can be obtained by dividing Equation 2.7 by its value in the absence of rotation, $\omega = 0$:

$$\bar{l_h} = \frac{l_{cr}}{l_{h,\omega=0}} = \sqrt{1 + (1+\mu_t^2)\alpha^2}. \tag{2.8}$$

This expression represents a basic theory for predicting the buckling length of a rod

undergoing rotation. This theory does not take into account changes in the critical buckling force due to twisting effects. A more sophisticated theory will be developed which takes these factors into account.

2.2.2 Extended Reach by Rotation: Advanced Theory

In the above section, an initial theoretical prediction of the buckling length of a rod undergoing continuous rotation was derived by considering only factors that increase reach with rotation. In this section, a more advanced theory is obtained that also considers factors that decrease reach.

A major assumption in the derivation of Equation 2.8 was that the critical buckling force remains constant in the presence of rotation. In reality, this is not true. There are two factors that act to decrease F_{cr} in the presence of rotation: i) reduction in normal force between the rod and the constraint and ii) presence of twist in the rod due to rotation. These two effects are taken into account in the following equation for the critical buckling force:

$$F_{cr} = F_{cr}(\alpha) = 2\sqrt{2}k(\alpha)\sqrt{\frac{EIN(\alpha)}{\Delta r}}, \tag{2.9}$$

where $k(\alpha) \leq 1$ represents a factor that takes into account the reduction in F_{cr} due to twisting and $N(\alpha)$ is the normal force between the rod and constraint defined in Equation 2.4. In order to account for the reduction in F_{cr}, Equations 2.9, 2.4, and 2.1 are inserted into Equation 2.7 to obtain an updated prediction for the normalized buckling length:

$$\bar{l_h} = \frac{l_{cr}}{l_{cr,\omega=0}} = k(\alpha)\left\{(1+\alpha^2)\left[\,1+(1+\mu_t^2)\alpha^2\,\right]\right\}^{1/4}. \tag{2.10}$$

This equation remains dependent on the twisting parameter, $k(\alpha)$. In order to calculate this value, the force equilibrium for a pure helix confined in a cylindrical

constraint is used [26]. This equation is copied here for convenience:

$$\frac{8\pi^4 EI}{P^4} = \frac{2\pi^2 F}{P^2} + \frac{4\pi^3 T}{P^3} - \frac{W}{\Delta r}. \tag{2.11}$$

Here, F is the end-to-end force applied to the helix in the axial direction, T is the torque applied to the helix, P is the helical pitch, and W is the weight per unit length. This equation is non-dimensionalized to become:

$$f = \frac{1}{2p^2} + \frac{p^2}{2} - \frac{t}{\sqrt{2}p}, \tag{2.12}$$

where $f = F/F_{cr,\omega=0,k=1}$ is the axial force non-dimensionalized by dividing by F_{cr} in the absence of rotation, $p = P/P_0$ is the helical pitch non-dimensionalized by a factor $P_0 = (8\pi^4 EI\Delta r/W)^{1/4}$, and $t = T/\sqrt{F_{cr,\alpha=0,k=1}EI}$ is the dimensionless torque. Equation 2.12 describes the axial force f required to maintain a helix of pitch p with applied torque t. Comparison of Equation 2.9 to the definition of the non-dimensionalized force reveals that f is equivalent to the reduction in the critical force due to twisting. It is, therefore, equal to the twisting parameter, $k(\alpha)$. In order to have a complete expression for F_{cr}, it is necessary to find an expression for $f = k(\alpha)$ that does not include t.

For a given value of t, Equation 2.12 can be used to calculate the minimum value of f required to form a helix. This is accomplished by finding the minimum value of f for which there is a non-imaginary solution for p by setting $df/dp = 0$ with a fixed value of t. This minimization yields:

$$f = \frac{\sqrt{2}}{\sqrt{t^2+8}-t} + \frac{\sqrt{t^2+8}-t}{4\sqrt{2}} - t\sqrt{\frac{\sqrt{2}}{\sqrt{t^2+8}-t}}. \tag{2.13}$$

In order to solve this equation, a relationship between t and f is required. This is found by examining the axial force and torque within the rod during injection. It has

already been shown above that the total axial force within the rod is given by:

$$F_a = \int_0^s f_a ds = f_a s. \tag{2.14}$$

It can similarly be shown that the total torque within the rod is given by:

$$T = \int_0^s f_t R\, ds = f_t R s. \tag{2.15}$$

Solving both equations for s, equating them, and inserting the same non-dimensional variables used in Equation 2.12 yields the desired relationship between t and f:

$$\frac{t}{f} = (32)^{1/4}\, \alpha\, \bar{\mu}\, \frac{R}{\lambda_b}, \tag{2.16}$$

where $\bar{\mu} = \mu_t/\mu_a$ and $\lambda_b = (4EI\Delta r/\rho g A)^{1/4}$ or the sinusoidal buckling length defined in Equation 1.3. It is possible to solve Equations 2.13 and 2.16 numerically to obtain an exact value for $f = k(\alpha)$. However, if the torque, t, is assumed to be small, it is possible to obtain the following solution using Taylor expansion:

$$f_{cr} = k(\alpha) = \frac{1}{1 + 8^{1/4}\alpha\, \bar{\mu}\, \xi_r}, \tag{2.17}$$

where $\xi_r = R/\lambda_b$. Inserting the expression for f_{cr} into Equation 2.10 gives:

$$\bar{l_h} \approx \frac{1}{1 + 8^{1/4}\alpha\, \bar{\mu}\, \xi_r} \left\{ (1+\alpha^2) \left[1 + (1+\mu_t^2)\alpha^2 \right] \right\}^{1/4}. \tag{2.18}$$

This equation represents an approximate prediction for the buckling length of a rotating rod within a cylindrical constraint that considers factors that both increase and decrease reach. It is important to note that while Equation 2.8 is independent of radial clearance and rod mechanical properties, Equation 2.18 includes dependence

on these parameters through the dimensionless parameter, ξ_r. Experimental work described in Chapter 3 validates these predictions as well as several assumptions made in their derivation.

Chapter 3

Reach Extension by Continuous Rotation

In this chapter, we present the methodology and results for our investigation of the buckling behavior of a rod injected into a cylindrical constraint while undergoing continuous rotation. The experiments were designed to test the merit of using rotation of a rod at its injection point to increase the length to which it can be injected into a horizontal cylinder. Concurrently, the experimental results were used to validate a theoretical framework for this problem as well as several assumptions utilized in its derivation. In § 3.1, we describe our experimental apparatus that was developed to provide simultaneous rotation and injection of a polymeric rod into a horizontal cylindrical constraint. Using this apparatus, four aspects of buckling behavior were explored: i) buckling length of the rod relative to the non-rotating case, ii) rotation speed of the rod tip relative to the driven rotation speed, iii) rise angle of the rod within the constraint, and iv) the effect of variable injection speed on buckling. In § 3.2, we present the results for these studies. The experiments presented were designed and implemented by the author over the course of this thesis work. As noted previously, the theoretical predictions are the work of Dr. Tianxiang Su of Schlumberger-Doll Research, which are provided and discussed in detail for the purpose of comparison.

3.1 Rotational Experimental Apparatus

We have developed a precision desktop scaled experimental apparatus with the primary goal of examining the effects of rotation on rod buckling length within a cylinder. In order to gain insight and a predictive understanding of these effects, we performed a systematic parametric exploration of the underlying physical parameters of the problem, namely: the rod rotation speed, the rod injection speed, and the friction coefficient of the contact between the rod and constraint. This required designing an apparatus capable of rotating the rod around its axis at a set constant speed, while injecting the rod into the constraint at a speed set independently of the rotation.

The apparatus, pictured in Figure 3-1, consisted of an injection head mounted within a rotating acrylic housing. This housing was rotated around its axis using a servo motor connected to the housing using a custom built gear transmission. Thus,

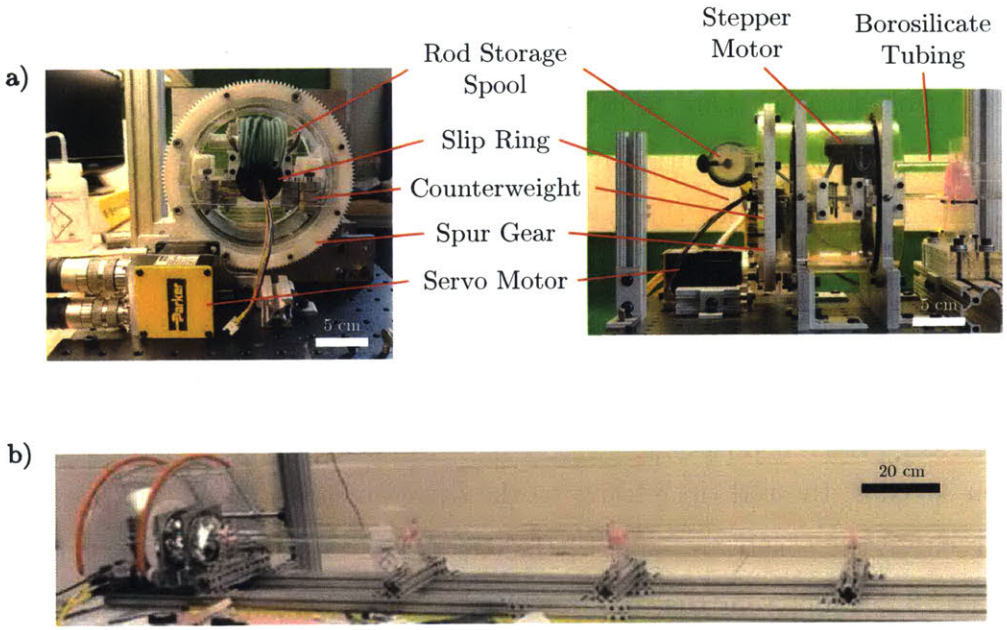

Figure 3-1: Rotational experimental apparatus. (a) Annotated photographs of rotation injection assembly (b) Photograph of entire experimental apparatus, including lengths of borosilicate tubing.

the overall design consisted of two main subsystems: the rotation drive system and the injection system. In combination, these subsystems allowed precision control of the experimental parameters, as is discussed in detail in the following subsections.

3.1.1 Rotational Drive System

The purpose of the rotational drive system was to axially rotate the rod during injection into the cylinder. This was accomplished by building a rotating housing into which an injection assembly could be mounted. A rendered computer aided design (CAD) model of the rotational drive system is shown in Figure 3-2. The housing consisted of a 15 cm long section of acrylic tubing with an outer diameter of 15.2 cm. This housing was constrained to rotate around its axis by mounting it into two bearings, which were carefully aligned concentrically with the housing to minimize rotational eccentricity. Three pairs of diametrically opposed acetal resin mounts were affixed to the inside surface of the acrylic housing to allow attachment of the injection assembly within the housing. The entire experimental apparatus was secured to a 12x12 inch optical breadboard for ease of positioning and alignment.

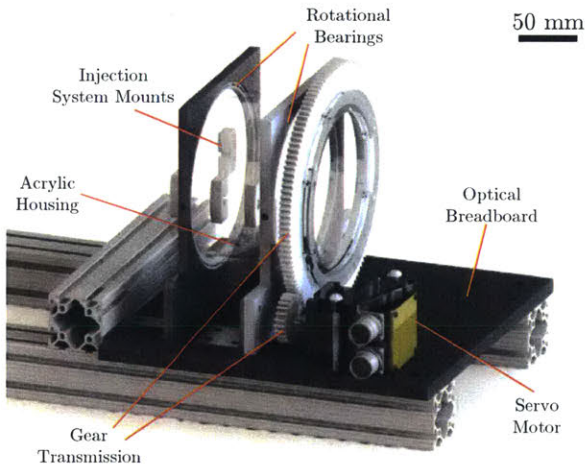

Figure 3-2: Rotational drive system CAD rendering. This subsystem consists of a rotating acrylic housing driven by a servo motor.

The axial rotation of the housing was provided by a servo motor [1] interfaced with the main housing using a simple custom built gear transmission. This transmission consisted of two gears: a large 132-tooth spur gear mounted concentrically with the acrylic housing and a smaller 24-tooth gear mounted to the motor shaft, creating a geared transmission with a 5.5:1 reduction. An on-board encoder included in the servo motor was used to track the velocity and position of the housing by dividing all measured values by the a factor of 5.5. The maximum rotational speed of the housing assembly was 300 rpm, which was limited by the maximum rated speed of the mounting bearings.

3.1.2 Injection System

The purpose of the injection system was to allow continuous insertion of a flexible elastomeric rod into the cylindrical constraint. A CAD rendering of this system is shown in Figure 3-3. The main body of the injection assembly consisted of a shelf designed to be inserted into the rotation drive assembly described in § 3.1.1. Components were attached to the shelf to facilitate injection and storage of the rod.

The rods used for these experiments were cast out of a vinyl polysiloxane (VPS) polymer injected into a length of straight 3.16 mm ID PVC tubing. This process allows for the creation of perfectly straight rods with known mechanical properties. A more detailed description of this casting process can be found in previous publications [27, 28, 29]. The mechanical properties of the rod used are listed in Table 3.1. Prior to experimentation, these rods were coated with chalk[2] to create a consistent frictional coating between the rod and the constraint. This was done by agitating the rod within a container filled with chalk. Excess chalk was then removed by first passing the rod through a compressed air stream followed by passing it between soft foam blocks. This process allowed for a consistent frictional coating between the rod and the constraint.

The rod was continuously inserted using a pinch-wheel style injector head similar

[1] Parker Motion BE230F DC Motor, Stall torque: 0.37 Nm.
[2] Irwin Strait-Line Standard

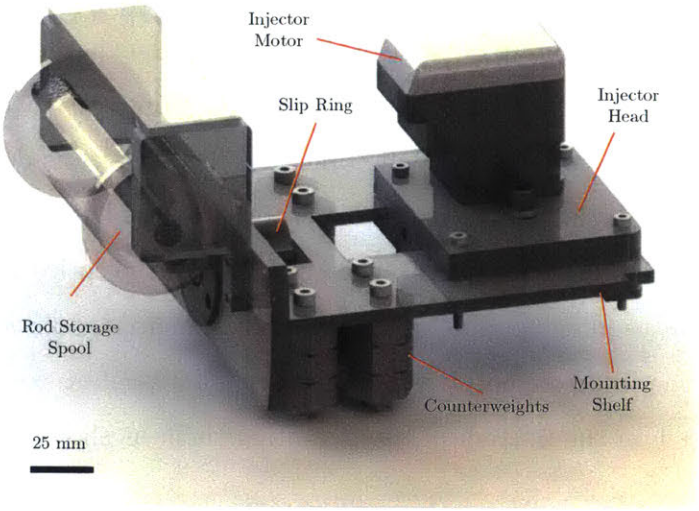

Figure 3-3: Injection system CAD rendering. This subsystem consists of an injection head mounted to a shelf allowing operation while undergoing continuous rotation.

Property	Value
Young's Modulus, E	1296 ± 31 $[MPa]$
Density, ρ	1210 ± 8 $[kg/m^3]$
Diameter, d	3.16 ± 0.05 $[mm]$
Poisson's Ratio, ν	0.49

Table 3.1: Relevant Rod Mechanical Properties

to those used in extrusion-type 3D printing devices. This injector head was powered using an injector stepper motor[3]. Using LabVIEW software, this motor allowed precise control of the injection velocity of the rod for values ranging from 0.1 cm/s to 10 cm/s. In order to minimize translational motion of the rod during insertion, the injector head was positioned so that the rod exited the injector along the axis of rotation of the housing assembly.

The rotary nature of the injection assembly apparatus produced several design challenges. First, it was necessary to wire all electronic connections to the injector head motor through a rotational slip ring. This rotary electrical connection allowed the injector head to revolve continuously without causing twisting and eventual failure of the electrical leads linking the motor to its power source and to the controlling

[3]Intelligent Motor Systems MDrive 14 Plus Motion Control

computer. In addition, it was necessary to store the rod within the injection system to prevent significant buildup of twist in the rod prior to experimental insertion. This was accomplished by mounting a rod storage spool onto the back of the injection assembly. Held in place by two acrylic brackets, this spool was designed to store up to 5 meters of rod during a continuous experimental run. Lastly, ensuring a constant axial rotation speed required that the center of mass of the entire assembly be as close to the axis of rotation as possible. This was accomplished by offsetting the relatively large mass of the injector motor with several counterweights, consisting of stainless steel nuts placed on the bottom of the mounting shelf, as shown in Figure 3-3.

3.1.3 Experimental Apparatus Implementation

When combined, the two subsystems described above formed the experimental apparatus used for the continuous rotation testing. The design of the apparatus permitted a wide range of values for both the injection speed $0.1 \leq v[\text{cm/s}] \leq 10$ and the rotation speed $0 \leq \omega[\text{rpm}] \leq 300$ of the rod. Detailed photographs of the assembled apparatus are shown in Figure 3-1. During experimentation, the apparatus was mounted on a structure consisting of four 1.21 m lengths of borosilicate tubing with equal diameters ranging from $12 \leq D[\text{mm}] \leq 34$, mounted end-to-end to create a single cylindrical constraint that was 4.84 m in length. The entire constraint was supported using a series of acrylic uprights with vinyl polysilicate rings placed at the tubing interfaces to reduce transmission of vibrations. The experimental apparatus was mounted at one end of this constraint, positioned so that the rod was injected at the bottom of the borosilicate cylinder, as shown in Figure 2-1.

3.2 Experimental Results

We proceed by describing the results of a series of experiments conducted using the apparatus described in § 3.1. The primary motivations of these experiments were to quantify and to understand the increase in buckling length gained by rotating a rod during injection into a cylinder. In addition to the buckling length experiments,

efforts were made to investigate the behavior of the rod during injection. A detailed understanding of this behavior is important for developing theoretical predictions of the effects of rotation on buckling length of rods. Additional experiments examined the transmission of twist along the length of the rod, the rise angle of the rod within the constraint, and the transverse coefficient of friction between the rod and constraint. The rods used in all these experiments had the geometric and mechanical properties listed in Table 3.1.

3.2.1 Buckling Length

As discussed in Chapter 1, the motivation behind this study was to identify methods of increasing the accessible distance into horizontal wellbores of coiled tubing. Specifically, we examined the helical buckling length, l_h, of a thin rod within a cylinder. Making use of the rotary experimental apparatus described above for this first series of experiments, we seek to provide evidence that continuous rotation of the rod results in significant increase in injection length prior to helical coiling.

During a typical experiment, the cylindrical constraint was filmed from above, beginning prior to the start of injection and ending after helical lockup. Using these videos, the precise times of key transitions in the rod, including the start of injection and the onset of helical buckling, could be determined (see §2 for details). This information, combined with the known injection speed of the rod, v, could then be used to determine the length of rod injected at these points. The results of these experiments can be seen in Figure 3-4 for a variety of clearances and injection parameters. Each data point represents the average value of 5 experiments conducted using the same independent parameters (clearance, injection speed, and rotation speed). The data is plotted as the normalized buckling length, $\bar{l_h}$, given by the ratio of l_h and the helical buckling length of the rod in the absence of rotation ($l_{h,\omega=0}$) as a function of the dimensionless velocity ratio,

$$\alpha = \frac{\omega R}{v}, \tag{3.1}$$

Here, R is radius of the rod (mm), ω is the rotation speed of the rod in units of (radians/s), and v is the injection speed (mm/s). As discussed in Chapter 2, the parameter α represents the ratio of the surface velocity of the rod due to rotation and the injection velocity.

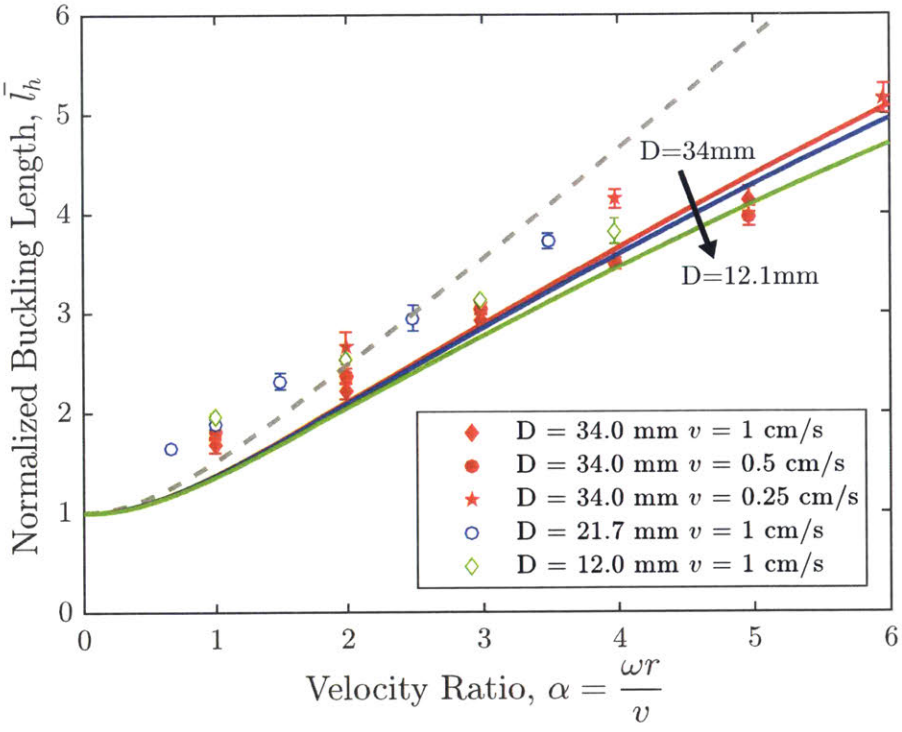

Figure 3-4: Rotational buckling length data. Experimental data for multiple constraint diameters and injection speeds. Dashed line represents the basic theoretical prediction accounting for transverse velocity and rise angle effects (Equation 2.8); solid lines represent the advanced theoretical prediction which also accounts for torsional effects (Equation 2.18) plotted for multiple constraint diameters and assuming anisotropic friction. Experimental data points represent average and standard deviation of 5 experimental results.

These experimental results show a direct relationship between $\bar{l}_h$ and α. It is important to note, however, that at the maximum value for the dimensionless velocity ratio, $\alpha = 6$, the normalized buckling length was as high as $\bar{l}_h = 5.1$, representing a significant increase in the horizontal reach of the rod into the pipe. In addition, the dimensionless parameters chosen allow the collapse of the experimental data points

into a single master curve, indicating that these parameters describe the system well.

The theoretical predictions compare well with the experimental data. The basic theory given by Equation 2.8, which accounts only for vector and rise angle arguments, approximates experimental values at lower values of α, however, it tends to increasingly overestimate these values at higher values of α. The more sophisticated theory given by Equation 2.18, which additionally takes into account torsional effects, eliminates this overestimation, resulting in an improved prediction of the experimental data. While this advanced theoretical prediction indicates some unaccounted for dependence on clearance, its effect appears to be relatively small compared to that of injection speed and rotation speed.

3.2.2 Rod Tip Rotation Speed

Upon completion of the buckling length experiments, it became necessary to examine several assumptions used to develop the theoretical predictions of buckling length described in § 2.2. The first assumption examined is that the axial rotation speed remains constant along the entire length of the rod. This was tested by measuring the rotation speed of the tip of the rod, Ω, over the course of an entire experiment and comparing it to the driven rotation speed at the injection site, ω.

This experiment was conducted by placing a circular ink mark approximately 1.5 mm in diameter on the surface of the rod next to the tip. The rod was then injected into the constraint with a set rotation speed until helical buckling occurred. All experiments were conducted with an injection speed of v =1 cm/s and constraint diameter of D =21.7 mm. During the entire injection process, the tip of the rod was followed with a camera capable of taking video at an accelerated frame rate of 120 frames per second. The video was processed to determine rotational period of the rod at approximately equally spaced times during the injection experiment. This was done by counting the number of frames required for the ink mark on the surface of the rod to complete one full rotation and using frame rate of the camera to convert this value to a rotational period in units of seconds. This process allows measurement of the rotational period of the rod to within $\pm$ 0.0083 s. In addition,

the video frame information was used to approximate the injected length of rod for each period measurement. Selected frames from an experimental video can be seen in Figure 3-5.

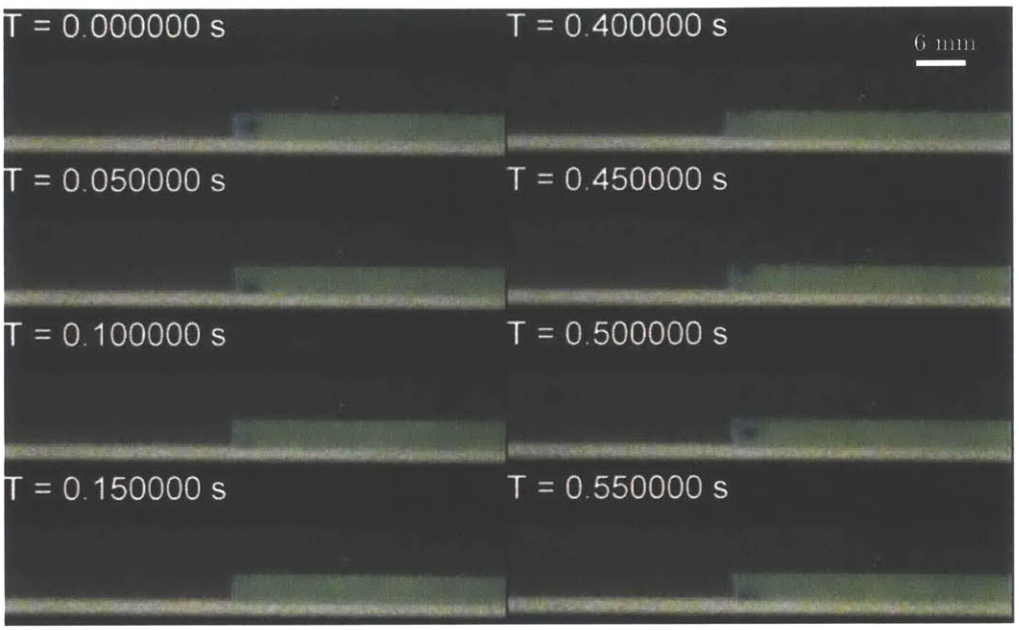

Figure 3-5: Sequence of frames illustrating the rotation of the tip during an experiment. This particular experiment has a driven frequency of $\omega = 120$ rpm and the original video was shot at 120 frames per second. Ink mark on the tip of rod requires 0.5 seconds to return to its center position indicating a tip rotation speed of 120 rpm.

Using this method, tip rotation data was collected for driven rotation speeds ranging from $60 \leq \omega[\text{rpm}] \leq 270$. Rotation period data was collected at approximately equal time intervals ranging from 12 to 23 seconds depending upon driven rotation speed with 5 full rotations observed at each point. After conversion from rotational period to rotation speed, this data was compiled and plotted as seen in Figure 3-6. This plot shows rod tip rotation speed as a function of injected length normalized by helical buckling length, $\bar{l}$, for a variety of driven rotation speeds.

There are several noteworthy features apparent in Figure 3-6. For the majority of observed points, the rotation speed remains relatively constant and equal to the driven rotation speed. This indicates that twist is transmitted from this injection site to the tip of the rod. However, at large values of driven rotation speed and normalized

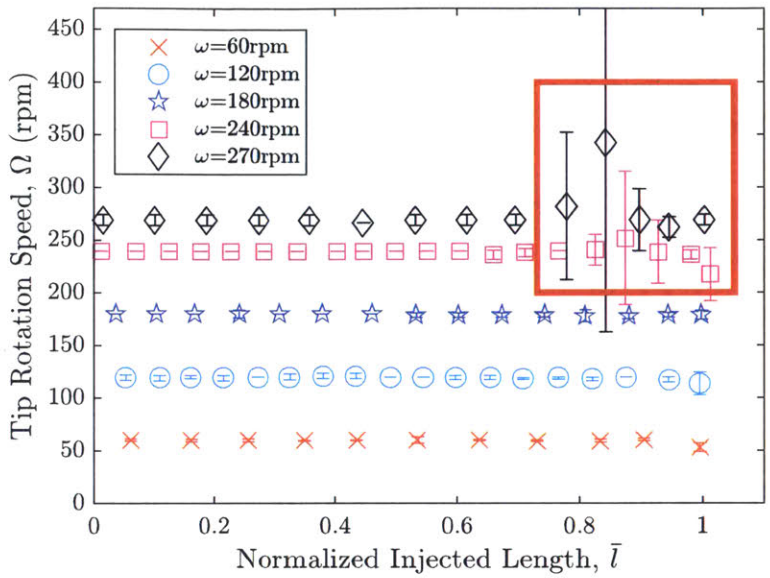

Figure 3-6: Tip rotation speed results. Rotation speed of rod tip for various injected lengths and driven rotation speeds. Highlighted region indicates data points where stick-slip was observed, resulting in relatively non-constant rotation speeds. Each data point represents the average and standard deviation of 5 measurements. All experiments were conducted with a constant injection speed of v =1 cm/s and clearance diameter of D =21.7 mm.

injected length, the tip rotation speed data becomes highly variable compared to the rest of the collected data. It was observed during experimentation that at these points, the rod tip would appear to go through periods of no rotation followed by rapid rotation in excess of the driven rotation speed. This indicates a periodic build up and rapid release of torsion within the rod. We hypothesize that this behavior is due to stick-slip occurring between the rod and constraint and is responsible for the high variability of the measurements in this region.

These findings indicate that for most of the parameters explored, twist is transmitted along the entire length of the rod. This supports the assumption that the rod is rotating at a constant velocity along its entire length. The stick-slip phenomenon observed at high values of normalized injected length and tip rotation speed indicate that this assumption may not be valid along the entire length of the rod for these parameters. In future implementations, this will be an important consideration when

using the theoretical predictions in § 2.2.

3.2.3 Rise Angle

As discussed in §2.2, constant axial rotation causes the rod to rise up the side of the constraint to a given angle, θ_r. This angle is given, at a location sufficiently far away from the injection site to ignore boundary effects, by Equation 2.3, repeated here for convenience.

$$\theta_r = \arctan(\mu_t) \tag{3.2}$$

where μ_t is the dynamic coefficient of friction between the rod and constraint in the transverse. The rise angle of the rod up the constraint is a key ingredient in the governing equations for the helical buckling length (see §2.2). It reduces the effective normal force between the constraint and rod, resulting in a decreased frictional force. We now describe a series of experiments designed to quantify the rise angle of the rod and compare the results to the theoretical prediction of its value.

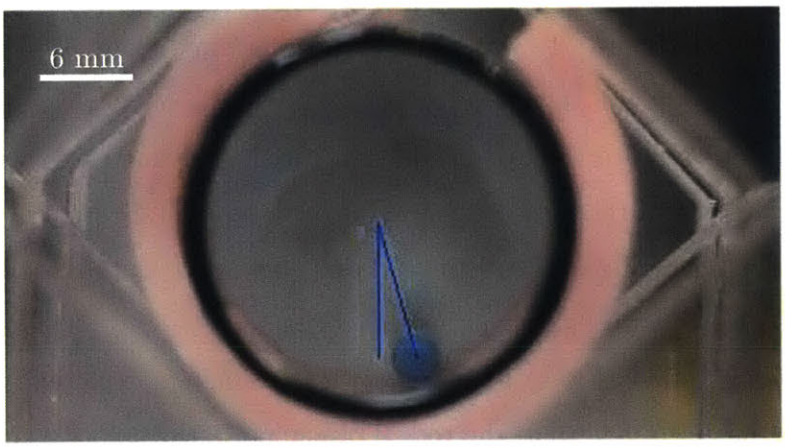

Figure 3-7: Rise angle experimental output. Sample frame from rise angle experimental video with measured rise angle indicated.

Experimentally, the rise angle of the rod tip was measured at an injected length sufficient to eliminate boundary effects from the injection site. In order to accom-

plish this, the length of borosilicate tubing comprising the cylindrical constraint was shortened to 1.21 m. The rod was then injected to a length of 1.2 m and rotated at a variety of speeds ranging from $60 \leq \omega$ [rpm] ≤ 300. While rotating, the rod tip was filmed using a camera aligned to the constraint axis. The position of the rod tip in this video was obtained using MATLAB point tracking software and the rise angle was calculated based on tip position relative to the center axis of the constraint. A sample experimental output is shown in Figure 3-7.

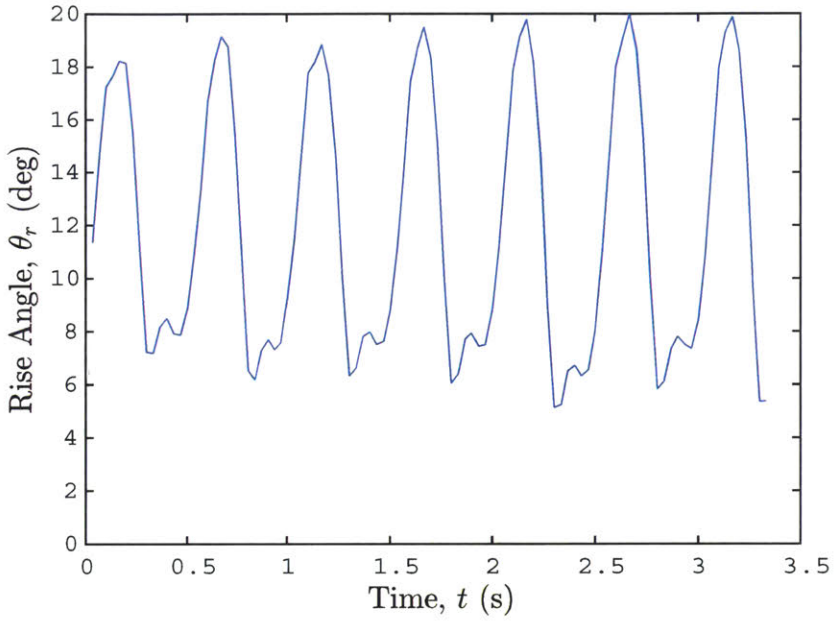

Figure 3-8: Plotted time-series of the rise angle, showing the periodic nature of rise angle in time. This particular experiment is at a driven rotational speed of ω =180 rpm.

The first significant finding of these experiments was that the rise angle does not remain constant with time as predicted by theory. Figure 3-8 shows the time series of the rise angle for a representative experiment (ω =180rpm). From this plot, it can be observed that the rise angle varies significantly and periodically with time. In order to further examine this periodic behavior, 20 rise angle measurements were taken at rotational speeds ranging from $40 \leq \omega$[rpm]≤ 240. For each of these measurements, a Fast Fourier Transform (FFT) was applied to the rise angle vs. time data for each

measurement and the results plotted in Figure 3-9, as a surface plot with normalized FFT amplitude displayed on the z (color) axis. The plotted solid line represents points where FFT frequency is equal to the driven rotational frequency. Additional dashed lines have been plotted to represent multiples of the driven frequency. These results indicate that the main frequency components in the rise angle vs. time data correspond to harmonics of the driven frequency, such that the periodic nature of this data can be attributed to rotational driving and not due resonant behavior of a constrained rod.

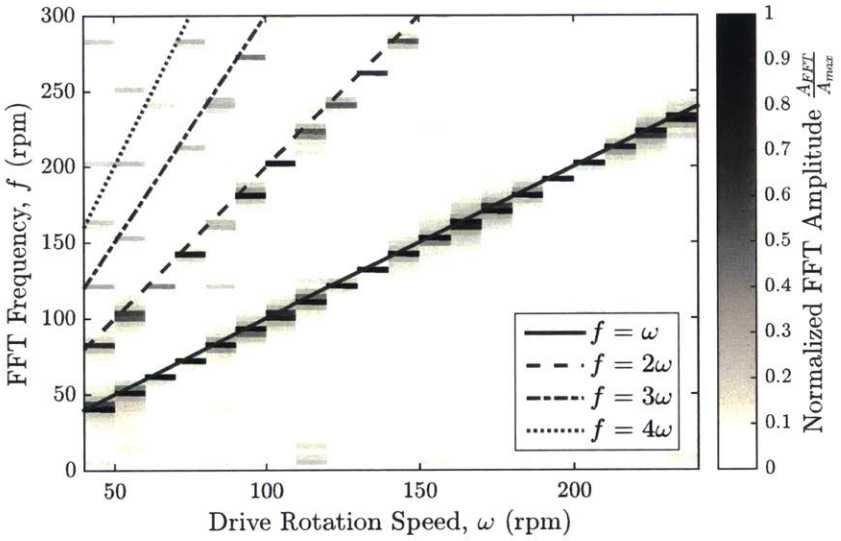

Figure 3-9: Surface plot showing FFT data for every driven frequency observed, normalized by the individual maximum peak values. Drawn lines indicate multiples of the driven frequency.

The second important finding of the rise angle data was that the average amplitude was much lower than predicted by Equation 2.3 when isotropic friction ($\mu_t = \mu_a$) is assumed. Figure 3-10 shows the average measured rise angle as a function of driven rotation speed. This data shows that the experimentally measured rise angles had an average rise angle magnitude of approximately 12°. This is significantly lower than the rise angle predicted by Equation 2.3 when using the previously measured value for the axial coefficient of friction in place of the transverse friction coefficient, $\mu_a = \mu_t = 0.54$ (dashed black line in Figure 3-10). These findings suggest that

the frictional contact between the rod and constraint is in fact anisotropic, meaning that the axial and transverse coefficients of friction have different values ($\mu_a \neq \mu_t$). Using the rise angle measurements shown in Figure 3-10 and Equation 2.3, an estimated value for the transverse coefficient of friction for the rods used in this experiment of $\mu_t \simeq 0.22$ was obtained. In order to verify these findings, the value of μ_t was independently verified using a secondary experimental apparatus that will be detailed in § 3.2.4.

The theoretical predictions described in § 2.2 rely on both the axial and transverse frictional coefficients. Proper use of these predictive equations both here and in future work will require a more complete understanding of the frictional contacts between the rod and the constraint.

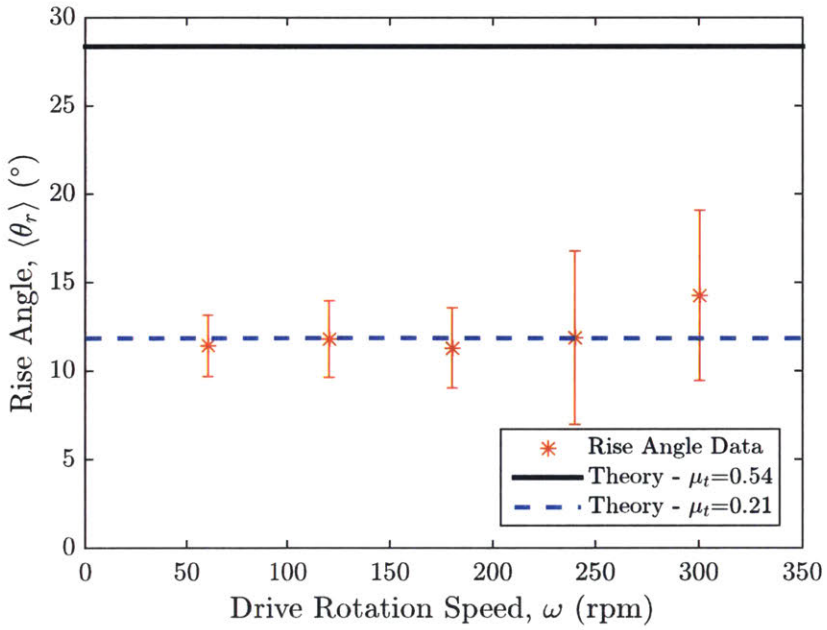

Figure 3-10: Rise angle data with theoretical prediction based on assumption of isotropic friction (black line) and an updated prediction taking into account anisotropy (blue line).

3.2.4 Friction Experiments

In order to experimentally verify the tangential coefficient of friction (μ_t) originally estimated from rise angle experiments in § 3.2.3, a second experimental apparatus was developed, photographs of which are shown in Figure 3-11. A static (non-injected) known length of rod was connected to a servo motor[4] and placed within a 40 cm length of 16.1 mm inner diameter borosilicate tubing of the same type used for the previous experiments. This tubing was mounted into a rotary air bearing, allowing free rotation in the axial direction with negligible rotational frictional forces. Also attached to this length of tubing is a force transmission arm designed to restrict axial rotation while transmitting torsional forces on the tubing to a precision laboratory scale placed below the experimental apparatus.

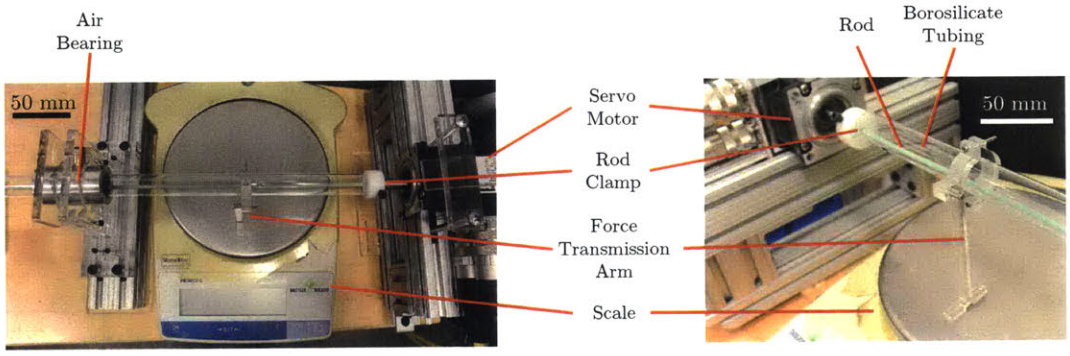

Figure 3-11: Photographs of the transverse friction measurement apparatus.

This device quantified the transverse frictional coefficient of the rod by measuring the torque imparted on the borosilicate tubing from an axially rotating rod. As shown in the schematic diagram of Figure 3-12, the servo motor was used to rotate the rod at a known rotation speed ω, causing it to rise up at an angle θ measured in the previous section.

While the rod was rotating, frictional contact between the rod and the constraint resulted in a torque being applied to the borosilicate tubing. The force transmission arm prevented the tubing from rotating due to this torque, causing a reaction force equal to the applied torque divided by the distance from the end of the force trans-

[4]Parker Motion BE230F DC Motor, Stall torque: 0.37 Nm

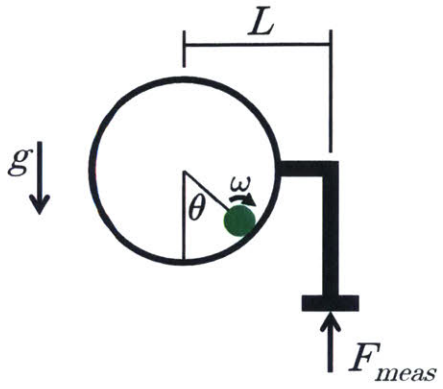

Figure 3-12: Schematic of transverse friction measurement.

mission arm to the center of the tubing, L. This reaction force, F_{meas}, was measured in standard units of mass to an estimated precision of $\pm 0.01g$ by the laboratory scale, then later converted to units of force. From this information, the transverse frictional coefficient could be calculated by:

$$\mu_t = \frac{2F_{meas}L}{\rho g cos(\theta) D A_{rod} l}, \tag{3.3}$$

where D is the diameter of the borosilicate tubing, A_{rod} is the cross sectional area of the rod, and l is the length of rod used. It is important to note that this equation does not rely on the rotational velocity, ω, of the rod.

Utilizing this apparatus for quantification of μ_t requires careful measurement of the reaction force generated on the force transmission arm. Prior to zeroing the laboratory scale, the rod was radially perturbed or "flicked" to ensure that it rested on the bottom of the tubing to eliminate residual rise angle effects from previous experiments. After zeroing the scale and ensuring that readings remained stable for a period of 15 seconds, the servo motor was set to spin at a specific velocity. After allowing an additional 15 seconds for the laboratory scale reading to ensure stabilization, the measured reaction force was recorded. This process was repeated for a variety of rod lengths and rotation speeds. The results of these experiments are plotted in Figure 3-13 with the measured value of μ_t plotted as a function of ω for four separate rods

ranging from 10 cm to 34 cm in length. The plotted lines represent the average and standard deviation of the measured values of μ_t. As expected, there was no apparent dependence of μ_t on rod length or rotation speed.

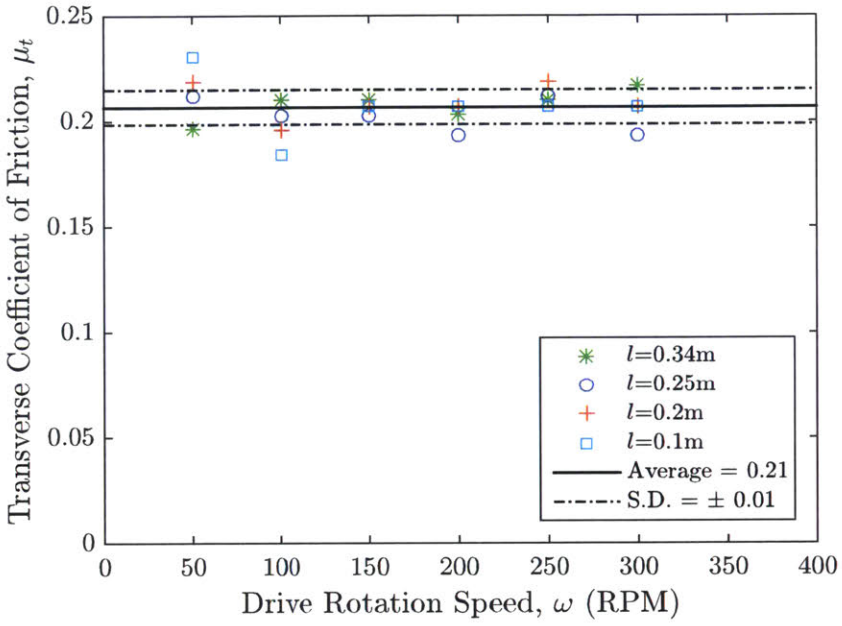

Figure 3-13: Friction measurement data. Results of experimental measurement of transverse friction coefficient, μ_t. Results indicate a coefficient of friction with a value of $\mu_t = 0.21 \pm 0.01$.

From this data, it can be observed that the measured values of $\mu_t = 0.22 \pm 0.01$ agree with the estimated value obtained from rise angle data in the previous section ($\mu_t = 0.21$). A revised prediction of the rise angle accounting for anisotropic friction is plotted in Figure 3-10 (blue line). While it has been shown that meticulous consideration of frictional anisotropy is necessary for future theoretical work, these results indicate that Equation 2.3 can be used to accurately predict rise angle, provided the appropriate component of the frictional coefficient is used.

3.2.5 Variable Injection Speed

During the course of the experiments described above, two interesting observations were made about the behavior of a helically buckled rod upon cessation of injection.

First, it was observed that if axial rotation of the rod continued once helical initiation was reached and the injection was stopped, the rod reverted from its helically buckled configuration back to the unbuckled, straight, configuration. Second, it was found that if injection was resumed after the rod had reverted to its straight configuration, it was possible to inject the rod an additional distance into the constraint prior to the recurrence of helical buckling. Since the primary goal of this work was to increase the length of rod injected into a cylindrical constraint prior to helical buckling, these observations merited further inquiry. The following series of experiments were conducted by Ryan McDermott (MIT Mechanical Engineering Class of 2015) and undergraduate researcher under direct supervision of the author.

The first experiments examined the time interval between cessation of injection and the reversion from helical buckling to an unbuckled configuration, which we shall refer to as the release time, t_r. The value of the t_r was measured for rod rotation speeds ranging from $5 \leq \omega[\text{rpm}] \leq 90$ and injected lengths ranging from $62 \leq l[\text{cm}] \leq 185$. In a typical experiment, the rod was injected to a known length prior to helically buckling, at which point rotation and injection were both stopped. The rod was then axially rotated at a set speed, ω, while being filmed from the top. The release time was then measured using knowledge of the video frame rate and the number of video frames between resuming rotation and complete reversion of the rod to its unbuckled state.

In Figure 3-14 we plot the results of these release time experiments for injected lengths ranging from $62 \leq l[\text{cm}] \leq 185$ and a rotation speed of ω =60rpm. Despite the scatter of the data, it appears that the release time tends to increase with injected length. This is likely due to the increase in frictional force resisting rod motion with higher injected lengths. It is also worth noting that the largest values of release times measured were approximately 10.5 seconds, a relatively short time compared to a typical injection experiment. Figure 3-15 shows a plot of the value of the release time at the constant injected length of $l = 79 \pm 6cm$ as a function of rod rotation speed (logarithmic scales). Plotted errorbars represent the standard deviation of 5 experimental values. The data is consistent with a power law relationship between

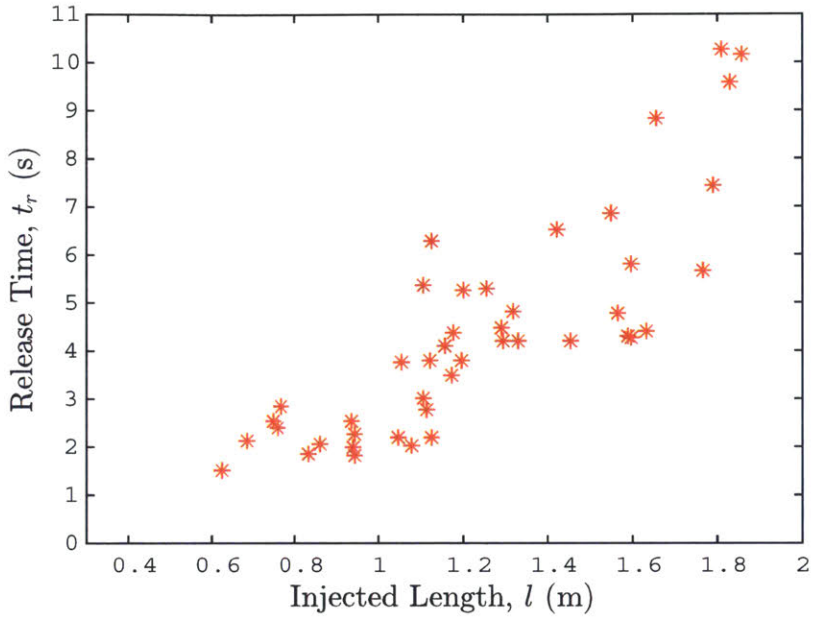

Figure 3-14: Release time results for a variety of injected lengths. Data taken for a rotation speed of ω =60rpm and a clearance diameter of D =21.7mm.

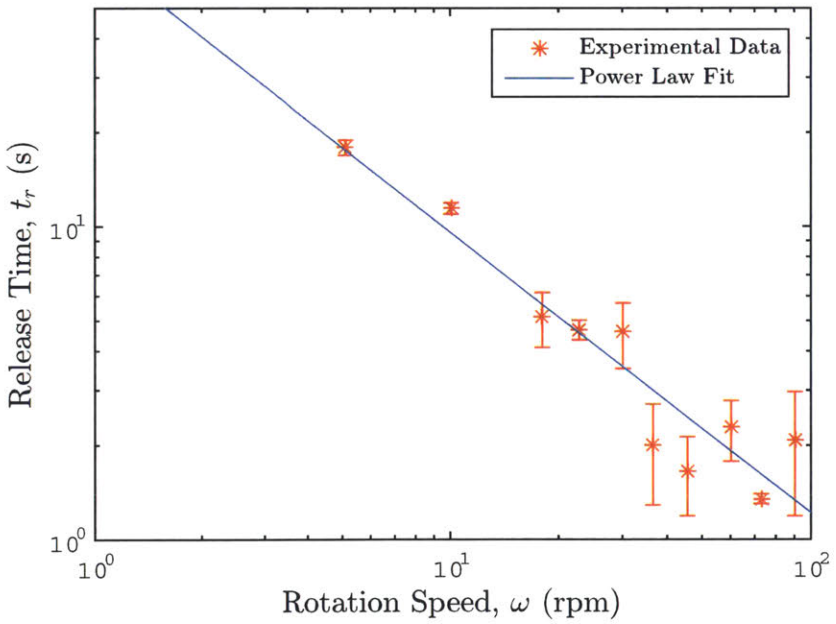

Figure 3-15: Plot of release time vs rotation speed. The plotted line represents a power law relationship of $t_r = 75.2\omega^{-0.895}$. This data was collected at an injected length of 79 $\pm$ 6 cm and a clearance diameter of 21.7 mm.

rotation speed and release time with release time decreasing with increasing rotation speed ($t_r = 75\omega^{-0.89}$).

The results of Figures 3-14 and 3-15 provide further insight into the factors affecting the release time. These plots show that release time increases with injected length and decreases with rotation speed. In order to fully understand this phenomenon, future work should focus on the effect of clearance diameter and the friction coefficient between rod and constraint on the value of the release time.

Next, we examine the effect that a non-constant injection rate has on the buckling length, $\bar{l}_h$. In these experiments, a rod rotating at $\omega = 60rpm$ was injected at a time varying velocity given as a square wave with an amplitude of 1 cm/s, a duty cycle of 0.50 and a set period, T. In Figure 3-16, the normalized buckling length, $\bar{l}_h$ is plotted as a function of the injection period, T. From this data, it can be observed that the presence of a non-constant injection speed results in an increase in the normalized buckling length. Interestingly, this effect appears to be highly dependent on the period, T, with the value of the normalized buckling length reaching its peak value

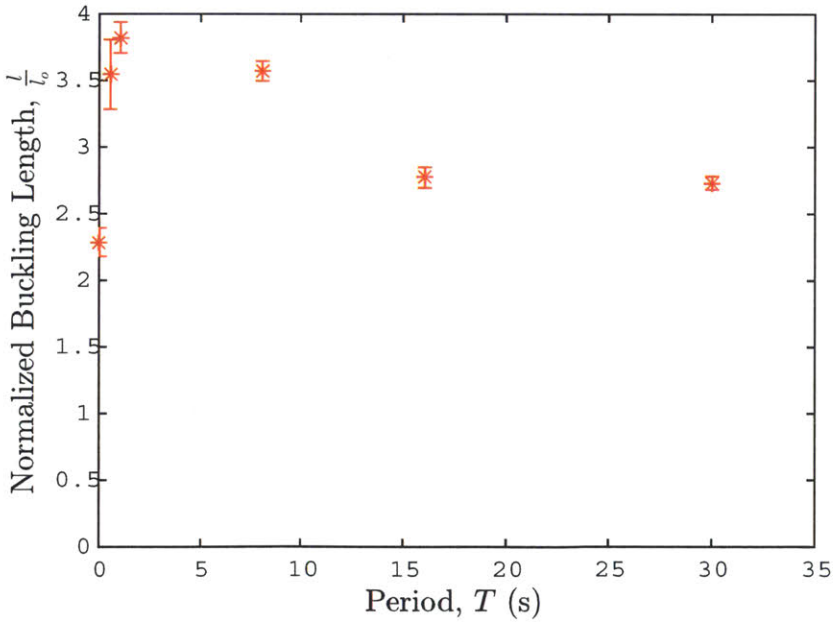

Figure 3-16: Buckling length vs. injection period. Data taken for a rotation speed of $\omega = 60rpm$ and a clearance diameter of 21.7 mm.

at a period of 1 second.

While this method of non-constant injection speed has the potential for improvements in buckling length it is unclear if there is any added benefit of a variable injection speed over injection at a slower constant speed. Injecting at a variable injection speed with a duty cycle of 0.5 effectively halves the injection speed and results in an 67 percent increase in buckling length. However, as shown in Figure 3-4, simply injecting at a constant velocity of half the original speed will increase buckling length by 100 percent. Future work on this subject should focus on the effects of rotation speed and clearance diameter in order to more fully understand this phenomenon and determine if it has any potential applications to the coiled tubing industry.

Chapter 4

Oscillatory Rotation

In this chapter, we present the methodology and results of experiments on the behavior of a rod undergoing oscillatory rotation while placed within a cylindrical constraint. As with the previous chapter, the ultimate goal of this work is to demonstrate the merit of oscillatory rotation as a possible means of reach extension in coiled tubing operations. In § 4.1, we present the experimental apparatus and results for an investigation of a static rod placed at the bottom of a cylindrical constraint while undergoing oscillatory rotation. In § 4.2, we present the experimental apparatus and results for a rod undergoing oscillatory rotations while being injected into the constraint.

4.1 Static Oscillation

Unlike the case of continuous rotation as studied in the previous chapter, a rod undergoing oscillatory rotation in a constraint is expected to demonstrate non-negligble dynamic resonant behavior. Developing an understanding of this resonance behavior is important for rationalizing the effects of oscillatory rotation on constrained buckling. Towards this goal, we have designed an experimental apparatus for the investigation of the resonant behavior of a static length of rod undergoing oscillatory rotation while placed at the bottom of a cylindrical constraint. This apparatus is capable of providing oscillatory rotations at a set frequency and amplitude while measuring the resultant lateral displacements of the rod within the constraint. In

Section 4.1.1, the experimental apparatus is described in detail. In Section 4.1.2, the methodology and results of several experiments conducted with this apparatus are reported.

4.1.1 Experimental Setup

For this investigation, an apparatus capable of providing oscillations of at least 50 degrees amplitude at frequencies in the range of 1-20 Hz was required.
Since the required amplitude and frequency is not within the working range of readily available servo motors, an alternative method of actuation was required. For this

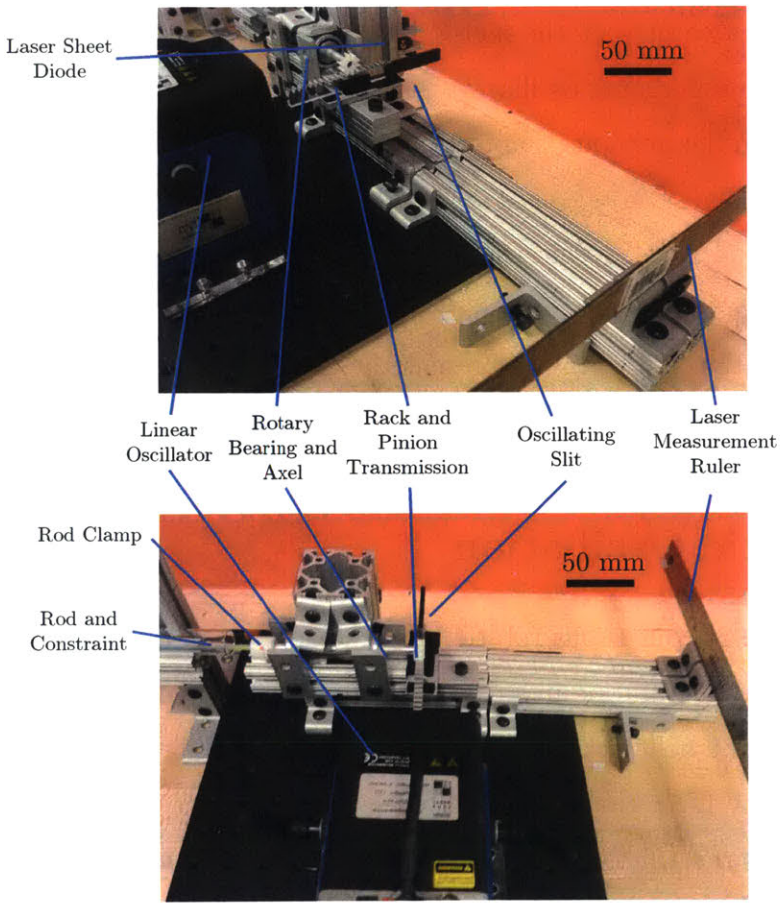

Figure 4-1: Photographs of static oscillation experiments. The apparatus consists of a linear actuator connected to a rack and pinion gear transmission. Linear oscillations are transformed into rotary oscillations through this transmission. Rotary oscillations are then transmitted to an elastomeric rod placed within a borosilicate tube.

experimental apparatus pictured in Figure 4-1, a linear oscillating shaker[1] capable of amplitudes of up to 13 mm was utilized. A rack and pinion gear transmission was used to convert linear oscillations from the shaker into rotary motion. Using an axle supported with two rotary ball bearings, the rotary motion was transmitted to a 30 cm length of rod clamped at one end of the axle. The rod was then inserted into a length of borosilicate tubing positioned to allow the rod to rest at the bottom of the tube for its entire length. As in the previous section, the rods used throughout this experiment were cast from a vinylpolysilicate polymer to a diameter of 3.16 mm.

The primary engineering challenge in assembling this experimental apparatus was development of a method to set and monitor the oscillation amplitude, as there is no reliable method to precisely control the amplitude of the shaker during oscillation. To solve this problem, a sheet style laser diode[2] was mounted onto the experimental apparatus with the laser plane oriented parallel to the table at a level which intersected the oscillating rack gear. As seen in the schematic diagram in Figure 4-2, an acrylic tab with a 0.5mm slit was mounted to the rack gear in front of the laser diode, blocking the majority of the laser light.

In the absence of linear oscillation, the projected laser pattern from this configuration forms a single point. However, when the slit begins to oscillate with the rack gear, the projection becomes a horizontal line. The projected length of this line is directly dependent on the oscillation amplitude of the slit. This pattern was projected onto a metric ruler placed 23.5 mm away from the oscillating slit.

In order to use the length of the projected laser pattern to measure rotational oscillation amplitude directly, a calibration was conducted at 10 equally spaced oscillation amplitudes, set by increasing the input voltage to the shaker in equal increments. At each point, the rotary oscillation amplitude of the rod clamp was measured by filming the clamp using a high speed camera [3] set to take video at an accelerated frame rate of 402 frames per second. The videos were processed using a custom MATLAB script

[1]The Modal Shop SmartShaker with integrated power amplifier (model K2007E01) magnet shaker with 21 N peak sine force, 13 mm continuous stroke, and frequencies up to 9 kHz

[2]650nm Wavelength, 120 degree fan arc

[3]Nikon N1J3 mirrorless DSLR camera

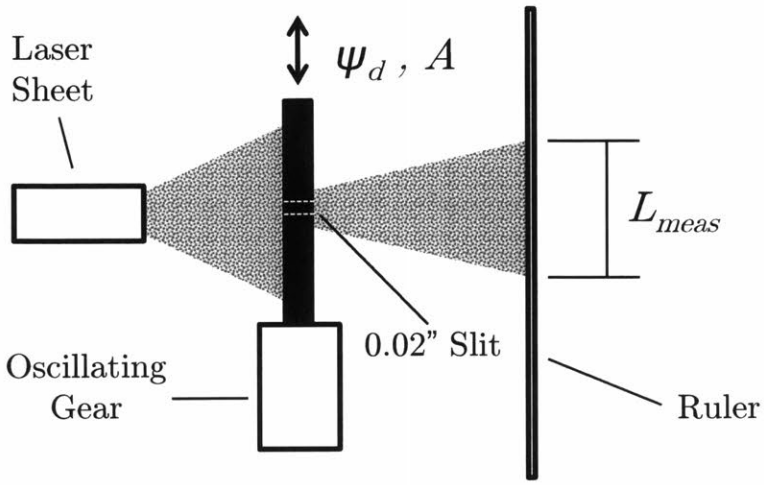

Figure 4-2: Diagram of laser sheet oscillation measurement system.

to determine oscillation amplitude in degrees. In addition, at each point, the length of the laser line (L_{meas}) projected onto the ruler was measured in mm. The error in this length measurement was estimated to be approximately ± 1 mm, primarily due to the lack of sharpness in the projected line ends. The calibration results are shown in Figure 4-3.

From the data in Figure 4-3, it can be seen that this method of measuring oscillation amplitude was successful. The relationship between oscillation angle and L_{meas} was found to be highly linear with an R^2 value of 0.999. The results of a linear fit to this data indicate that the relationship between oscillation amplitude and projected laser length is:

$$\theta_r = 14.38 L_{meas} - 2.52 \tag{4.1}$$

Throughout experimentation, Equation 4.1 was utilized to set rotary oscillation amplitude.

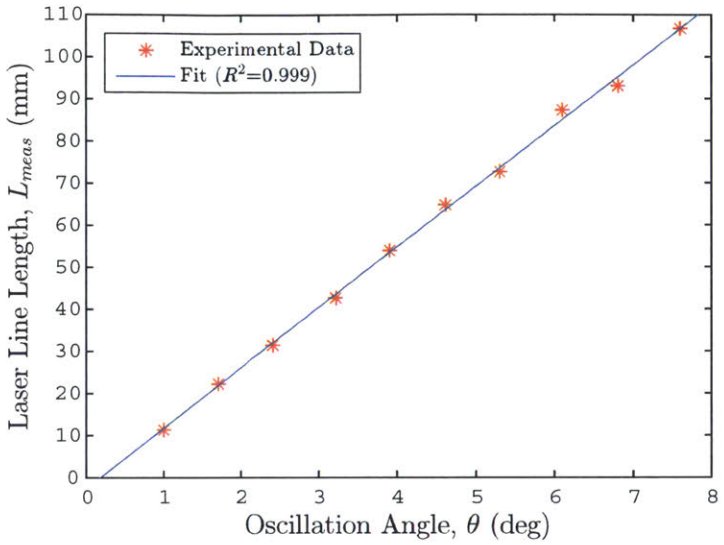

Figure 4-3: Laser sheet oscillation measurement calibration. Calibration for using laser sheet to measure rotary oscillations. Data is fit to a line of $\theta_r = 14.38L_{meas} - 2.52$ ($R^2 = 0.999$).

4.1.2 Results

In this section, we present the experimental methods and results for experiments conducted on the apparatus described in Section 4.1.1. The main focus of this investigation was to examine the resonant behavior of a rod undergoing oscillatory rotations within a cylindrical constraint. This was accomplished by exciting the rod with oscillations of set amplitude (A) and varying driving frequencies (ψ_d), then measuring the output radial displacement of the rod (δx).

Rod displacement was measured for an 8-cm section of rod located 15 cm from the rod clamp. Displacement was measured by backlighting the rod and constraint using a LED light panel, then filming the rod displacements from above using a camera [4] at 402 frames per second. These videos were then processed using a MATLAB script to measure of rod radial displacement at approximately 330 points along selected length of rod.

Using this method, the radial displacement of the rod within its constraint was measured for rotational oscillations of amplitudes of $\theta_{ptp} = 75^o$ for driven frequencies

[4]Nikon N1J3 mirrorless DSLR camera

$1 \leq \psi_d[\text{Hz}] \leq 20$ and clearance diameters $6.7 \leq D[\text{mm}] \leq 21.7$. In these experiments, for a given clearance, the first frequency measured was 1 Hz after which the frequency was incrementally increased for each additional experimental run. For each set of parameters, an average peak-to-peak value of radial displacement (δx_{ptp}) was calculated along the entirety of the observed section of rod.

The plot in Figure 4-4 shows the average measured peak-to-peak displacement of the rod as a function of ψ_d for all 5 constraint diameters examined. From this it can be observed that there is significant resonant behavior in this system. For each diameter measured, the displacement observed at the resonant peak in the 7-13 Hz range is approximately 6 times higher than the displacement observed at the upper and lower limits of driven frequency. It was hypothesized that this behavior could be described by the equation governing the resonance of a sphere oscillating in a cylindrical channels given by:

$$\psi_n = \frac{1}{2\pi}\sqrt{g}\Delta r \tag{4.2}$$

The measured resonant frequencies (at which the maximum amplitudes from the

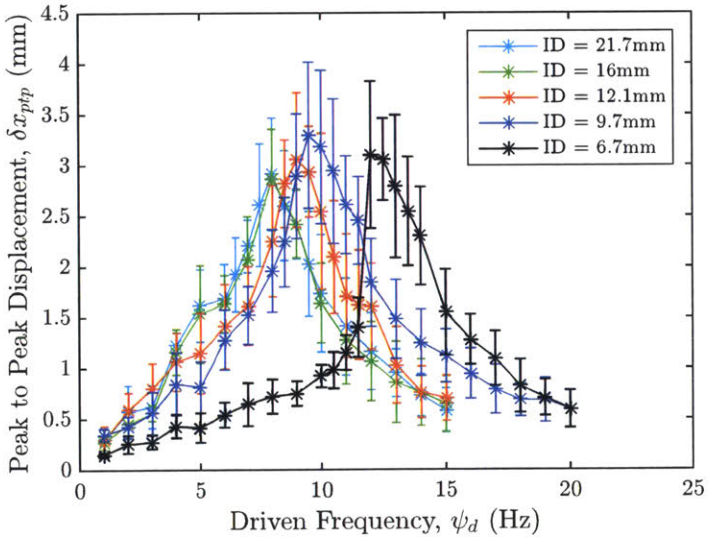

Figure 4-4: Resonance curve plot. Plots of radial displacement vs. frequency for various clearances. A clear resonance behavior is observed.

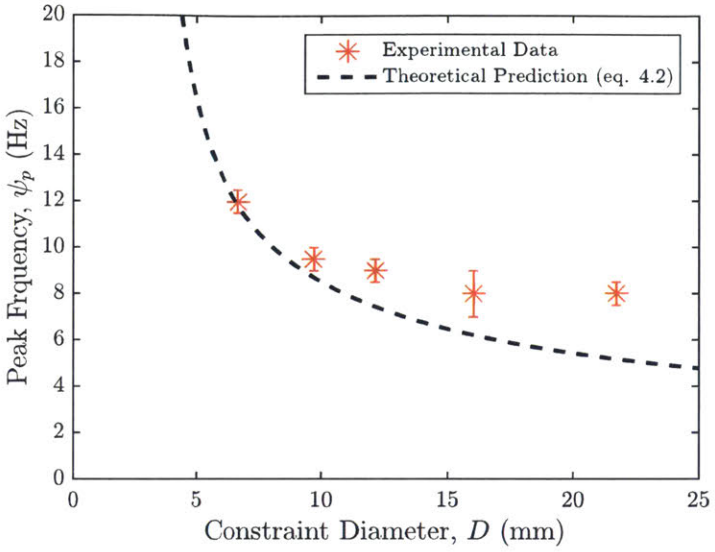

Figure 4-5: Comparison of experimentally observed peak location to theory. Experimentally observed peak location compared to prediction by Equation 4.2.

data in Figure 4-4 are plotted in Figure 4-5 as a function of constraint diameter and compared to Equation 4.2 finding that it provides a good approximation of the experimentally observed peak locations especially at low constraint diameters. However, as the clearance diameter increases, this equation increasingly underestimates peak location. This disagreement between prediction and measured values indicates that this resonant behavior is more complex than originally expected, presumably due to the nonlinearites introduced by the constraint and the geometry of the rod. This would be an interesting topic for future investigation.

4.2 Rotary Oscillation with Injection

Having gained physical insight into the behavior of a constrained rod undergoing axial rotary oscillations, we proceeded by examining the feasibility of axial rotary oscillation as a method for improving reach extension of coiled tubing in a cylinder. For this purpose, we designed an apparatus that allows simultaneous rotary oscillation and injection of a rod into a cylindrical constraint. Using this apparatus, a series of experiments into the helical buckling length of a rod undergoing axial rotary os-

cillations were conducted, similar to those that investigated continuous rotation and injection.

4.2.1 Experimental Apparatus

In order to conduct these experiments, a device capable of injecting a rod into a constraint while creating rotary oscillations with at least 50 degrees peak-to-peak amplitude at a frequencies as high as 15 Hz was required. A photograph of the final design is shown in Figure 4-6. The apparatus consists of a pinch-wheel injector head mounted on a rotating frame supported by two mounting bearings. The injection channel of this injector head was carefully aligned with a 3.5 mm hole drilled through the axis of rotation of the frame to allow a rod to be passed through the apparatus during injection. At the injection end of the frame, the rod passes through a pinch roller mechanism to clamp the rod, thereby eliminating twisting within the apparatus and ensuring that the oscillation amplitude of the rod at the injection site remains constant. Oscillation is provided by an electromagnetic shaker [5] connected to the frame by a rack and pinion gear transmission responsible for converting linear oscillations into rotary motion. In order to set the amplitude of oscillation to a

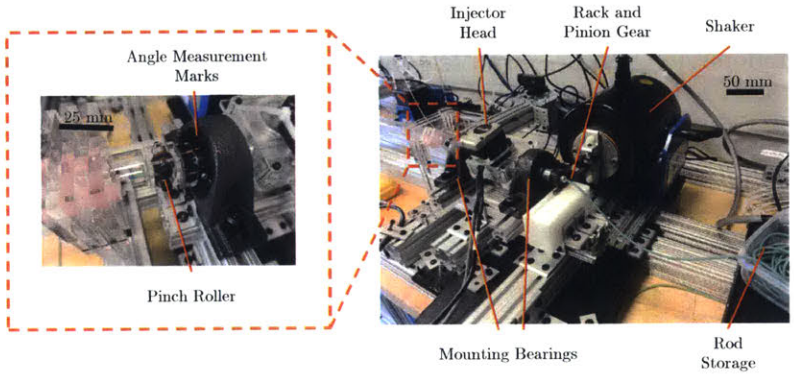

Figure 4-6: Experimental apparatus for rotary oscillation with injection. A pinch-wheel injector head is mounted onto a rotating frame with a rod injection channel drilled along the axis of rotation. An electromagnetic shaker connected to a rack and pinion gear transmission provides the oscillatory rotations.

constant peak-to-peak amplitude of 50 degrees, two red angle measurement marks

[5] The Modal Shop model 2075E shaker with 334N peak force

were placed 50 degrees apart on one of the mounting bearings. During operation, the rotary motion of these measurement marks causes them to appear as blurred lines. The oscillation amplitude is then increased until these lines appear to meet. At this point, the peak-to-peak oscillation amplitude is equal to the distance between the two marks, in this case 50 degrees. This process can be seen in Figure 4-7.

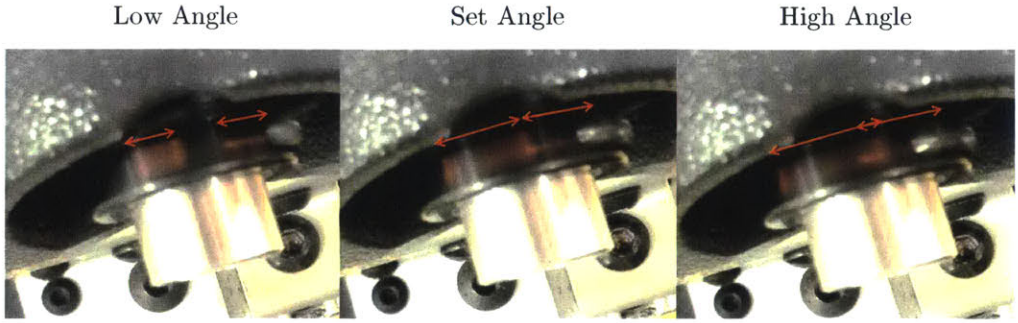

Figure 4-7: Angle measurement illustration. During operation, the two angle measurement marks (highlighted by red arrow) appear to become red blurred lines. a) At angles lower than the operating amplitude, these lines appear separate. b) At the set amplitude, they appear to meet. c) At angles higher than the set amplitude, they appear to overlap.

4.2.2 Experimental Methods

The procedures followed using the apparatus developed for buckling length experiments of the current chapter were similar to those of in Chapter 3 for continuous rotation investigation. In a typical buckling length experiment, the apparatus was placed at one end of the constraining pipe, which consisted of two cylindrical borosilicate tubes placed end to end to form a continuous channel. Each individual tube was 1.21 m in length and 21.7 mm in diameter. The injection site of the apparatus was positioned so that the rod was injected onto the bottom of the borosilicate constraint. Prior to injection, the rod was treated with chalk and the constraint was cleaned with ethanol to ensure a consistent frictional contact between the rod and constraint. The rod was injected into the constraint at a constant injection velocity set in the range of $0.25 \leq v[\text{cm/s}] \leq 1$, while undergoing rotary oscillations at a constant peak-to-peak amplitude, $\theta_{ptp} = 50^o$ and frequency,$4 \leq \psi_d[\text{Hz}] \leq 15$.

During experimentation, the rod was filmed from the side, near the injection site. The videos generated were later processed to determine the time difference between the start of injection to onset of helical buckling. Using the known injection speed of the rod, this time interval can then be used to determine the length of rod that had been injected at onset of buckling, l_h.

4.2.3 Results

In Figure 4-8, the results of these experiments are plotted as the buckling length normalized by the static buckling length, $\bar{l}$, as a function of the driven frequency, ψ_d, normalized by the resonant frequency measured for a 21.7-mm diameter cylindrical constraint (see Figure 4-5). From this plot, it can be observed that for frequencies lower than the resonant frequency, rotational oscillation increases buckling length by

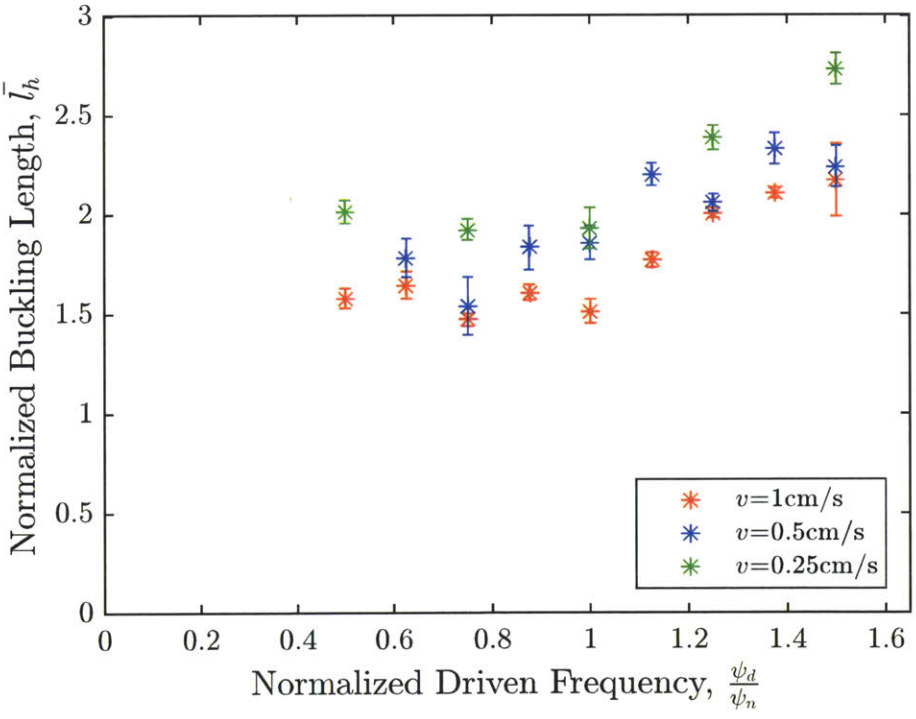

Figure 4-8: Rotary oscillation buckling length results. Normalized buckling length, $\bar{l}_h$ as a function of normalized frequency. Results measured for injection speeds $0.25 \leq v[\text{cm/s}] \leq 1$ and driven frequencies $4 \leq \psi_d[\text{Hz}] \leq 12$. In all experiments, the constraint diameter was D =21.7mm.

an average of 1.75 times when compared to the static case, with no apparent dependence on frequency. However, for frequencies higher than the resonant frequency, the buckling length appears to increase linearly with increasing frequency. In addition, there appears to be a slight dependence between buckling length and injection speed, with slower injection speeds typically resulting in higher buckling lengths. However, this dependence was not as significant as that observed for continuous rotation.

These experimental results indicate that rotational oscillation is capable of providing extension in helical buckling length of a rod in a cylindrical constraint. Within the range measured during the investigation, this extension reached as high as 2.4 times the static buckling length. These increases in buckling length achieved with oscillatory rotation are similar in magnitude to those observed by Miller et al. in the case of distributed vibration [12]. However, they are notably lower than the 5.1-fold increase observed for continuous rotation. Further studies examining the effects of clearance diameter, oscillation amplitude, and higher frequency oscillations will be necessary to more thoroughly understand this phenomenon and evaluate its relevance for potential applications to reach extension of coiled tubing.

Chapter 5

Conclusions and Future Work

We have presented an investigation into the effects of axial rotation on the helical buckling length of a slender rod injected into a cylindrical constraint. The primary motivation for this work was to gain physical insight into the conditions that can lead to extended reach of coiled tubing in horizontal wellbore operations. Toward this goal, two distinct modes of axial rotation of a slender rod during injection into a cylindrical constraint were examined: *continuous rotation* (Chapter 3) and *oscillatory rotation* (Chapter 4). For each of these modes of axial rotation, precision experimental apparatuses were constructed to allow for a systematic investigation of the effects on the buckling behavior.

Continuous Rotation: An apparatus was designed and built to provide simultaneous continuous axial rotation and injection of a polymeric rod into a length of borosilicate tubing. First, this apparatus was used to quantify the increase in helical buckling length produced with continuous rotation at various injection and rotation speeds. The results indicated that continuous rotation was able to provide increases in buckling length by as much as a factor of approximately 5 within the parameter range studied, when compared to the case of injection without rotation. These findings suggest the potential for significant benefits for coiled tubing reach extension. These experimental results were compared to theoretical predictions developed by Dr. Tianxiang Su at Schlumberger-Doll Research, which helped rationalize the problem. Excellent agreement was obtained between theory and experiments. Next,

three assumptions required in the derivation of this theory were experimentally verified. First, it was shown that for the majority of parameters explored, the injected rod maintains a constant rotation speed along its length. However, at high values of rotation speed and injected length, stick-slip dynamics caused increased variability in rod rotation speed. Secondly, we examined the angle at which the rod rises within the constraint due to axial rotation, which is an important ingredient in the theory. There were some discrepancies between these results and those predicted by theory. While theory predicted that the rise angle should remain constant in time, the experimental results showed significant temporal variability. In addition, the average measured rise angle was significantly lower than predicted by theory. It was hypothesized that this decrease in measured rise angle was due to the presence of unaccounted for anisotropy in the coefficient of friction between rod and constraint. Thirdly, to test this hypothesis, we measured the value of the coefficient of friction perpendicular to the axis of the rod, and found that it was approximately 60 percent lower than the friction coefficient in the axial direction, thereby indicating that the coefficient of friction of the rod was indeed anisotropic.

Oscillatory Rotation: Two apparatuses were developed to examine the effects of oscillatory rotation on a cylindrically constrained rod. The first of these allowed oscillatory rotation of a fixed length of rod within a borosilicate tube. With this setup, the frequency response of the lateral motion of a rod undergoing oscillatory rotation at constant amplitude was measured. The results demonstrated significant resonant behavior, with the value of lateral displacement rising to a definite peak at a specific resonant frequency. The values of these resonant frequencies were compared to a theoretical prediction based on resonance of a sphere rolling on cylindrical constraints of varying diameters. This comparison indicated some agreement between experiments and theory, with increasing divergence as tubing diameter increased. The second apparatus was built to study simultaneous oscillatory rotation and injection of a rod into a cylindrical constraint. The increase in helical buckling length was measured for a rod undergoing constant amplitude oscillatory rotation at a variety of frequencies and injection speeds. It was shown that oscillatory rotation was able to provide an

increase in buckling length by as much as a factor of 2.75, when compared to the non-rotating case. While this indicates possibilities for reach extension in coiled tubing operations, the expected gains do not appear as promising as what one may be able to achieve with continuous rotation.

5.1 Future Work

There are several possible avenues for future work in this area of study.

Continuous rotation: We were able to examine the effects of varying rotation speed, injection speed, and cylindrical constraint diameter on buckling behavior. However, there are other factors that will, likely, also have significant effects on buckling, including: the coefficient of friction between the rod and the constraint, the elastic modulus and natural curvature of the rod, and the tortuosity of the constraint. Investigation into the effects of these parameters on the buckling behavior of an axially rotating rod would add significantly to our understanding of this phenomenon.

Oscillatory Rotation: Some of the parameters that remain unexplored include constraint diameter, rod properties, and oscillation waveform. In addition, developing a more thorough physical understanding of the propagation of oscillatory rotations down the rod would be of significant interest. To date, a theoretical framework has not yet been developed to predict the increase in buckling length provided by oscillatory rotation. This would be another avenue for future studies that would be valuable to better understand and predict reach extension in coiled tubing operations.

Bibliography

[1] G. Brusco, P. Lewis, and M. Williams, "Drilling straight down," *Oilfield Rev.*, vol. 16, no. 3, pp. 14–17, 2004.

[2] V. P. Gupta, A. H. Yeap, K. M. Fischer, R. S. Mathis, M. J. Egan, *et al.*, "Expanding the extended reach envelope at chayvo field, sakhalin island," in *IADC/SPE Drilling Conference and Exhibition*, Society of Petroleum Engineers, 2014.

[3] G. W. P. Council, *Modern Shale gas development in the United States: a primer.* US Department of Energy, Office of Fossil Energy, 2009.

[4] B. Bennetzen, J. Fuller, E. Isevcan, T. Krepp, R. Meehan, N. Mohammed, J.-F. Poupeau, and K. Sonowal, "Extended-reach wells," *Oilfield Rev.*, vol. 22, no. 3, pp. 4–15, 2010.

[5] A. Acock, T. ORourke, D. Shirmboh, J. Alexander, G. Andersen, T. Kaneko, A. Venkitaraman, J. Lopez-de Cardenas, M. Nishi, M. Numasawa, K. Yoshioka, A. Roy, A. Wilson, and A. Twynam, "Practical approaches to sand management," *Oilfield Rev.*, vol. 16, no. 1, pp. 10–27, 2004.

[6] A. Afghoul, S. Amaravadi, A. Boumali, J. Calmeto, J. Lima, J. Lovell, S. Tinkham, K. Zemlak, and T. Staal, "Coiled tubing: The next generation," *Oilfield Rev.*, vol. 6, no. 4, pp. 9–23, 1994.

[7] I. McCourt, T. Truslove, and J. Kubie, "Penetration of tubulars into horizontal oil wells," *Proc. Inst. Mech. Eng., Part C*, vol. 216, no. 12, pp. 1237 1245, 2002.

[8] W. van Adrichem and K. Newman, "Validation of coiled-tubing penetration predictions in horizontal wells," *J. Pet. Technol.*, vol. 45, pp. 155–159, February 1993.

[9] I. McCourt and J. Kubie, "Limits on the penetration of coiled tubing in horizontal oil wells: Effect of the pipe geometry," *Proc. Inst. Mech. Eng., Part C*, vol. 219, no. 11, pp. 1191–1197, 2005.

[10] K. Bhalla, "Coiled tubing extended reach technology," in *Offshore Europe*, Society of Petroleum Engineers, 1995.

[11] A. M. Al Shehri, S. M. Al-Driweesh, M. Al Omari, and S. Al Sarakbi, "Case history: Application of coiled tubing tractor to acid stimulate open hole extended reach power water injector well," *SPE paper*, vol. 110382, 2007.

[12] J. T. Miller, C. G. Mulcahy, J. Pabon, N. Wicks, and P. M. Reis, "Extending the reach of a rod injected into a cylinder through distributed vibration," *J. App. Mech.*, vol. 82, no. 2, p. 021003, 2015.

[13] L. J. Leising, E. C. Onyia, S. C. Townsend, P. R. Paslay, D. A. Stein, *et al.*, "Extending the reach of coiled tubing drilling (thrusters, equalizers and tractors)," in *SPE/IADC drilling conference*, Society of Petroleum Engineers, 1997.

[14] E. K. Bassett, A. H. Slocum, P. T. Masiakos, H. I. Pryor, O. C. Farokhzad, and J. M. Karp, "Design of a mechanical clutch-based needle-insertion device," *Proc. Natl. Acad. Sci*, vol. 106, pp. 5540–5545, August 2009.

[15] D. Svenšek and R. Podgornik, "Confined nanorods: Jamming due to helical buckling," *Phys. Rev. E*, vol. 77, p. 031808, Mar 2008.

[16] W. Klug, M. Feldmann, and M. Ortiz, "Three-dimensional director-field predictions of viral dna packing arrangements," *Computational Mechanics*, vol. 35, no. 2, pp. 146–152, 2005.

[17] A. Lubinski, "A study of the buckling of rotary drilling strings," *Drilling and Production Practice*, pp. 178 214, 1950.

[18] A. Lubinski and W. Althouse, "Helical buckling of tubing sealed in packers," *J. Pet. Technol.*, vol. 14, pp. 655–670, June 1962.

[19] N. Wicks, B. L. Wardle, and D. Pafitis, "Horizontal cylinder-in-cylinder buckling under compression and torsion: Review and application to composite drill pipe," *International Journal of Mechanical Sciences*, vol. 50, no. 3, pp. 538 – 549, 2008.

[20] J. Miller, T. Su, J. Pabon, N. Wicks, K. Bertoldi, P. Reis, *et al.*, "Buckling-induced lock-up of a slender rod injected into a horizontal cylinder," *Int. J. Solids Struct.*, vol. 72, pp. 153–164, 2015.

[21] P. Paslay and D. Bogy, "The stability of a circular rod laterally constrained to be in contact with an inclined circular cylinder," *J. App. Mech.*, vol. 31, no. 4, pp. 605–610, 1964.

[22] R. Dawson, "Drill pipe buckling in inclined holes," *J. Pet. Technol.*, vol. 36, no. 10, pp. 1–734, 1984.

[23] Y. Chen, Y. Lin, and J. Cheatham, "Tubing and casing buckling in horizontal wells (includes associated papers 21257 and 21308)," *J. Pet. Technol.*, vol. 42, no. 2, pp. 140 141, 1990.

[24] I. McCourt, T. Truslove, and J. Kubie, "On the penetration of tubular drill pipes in horizontal oil wells," *Proc. Inst. Mech. Eng., Part C*, vol. 218, no. 9, pp. 1063–1081, 2004.

[25] Y.-C. Chen, Y.-H. Lin, and J. B. Cheatham, "Tubing and casing buckling in horizontal wells (includes associated papers 21257 and 21308)," *J. Pet. Technol.*, vol. 42, no. 02, pp. 140–191, 1990.

[26] S. Miska and J. Cunha, "An analysis of helical buckling of tubulars subjected to axial and torsional loading in inclined wellbores," in *SPE Production Operations Symposium*, Society of Petroleum Engineers, 1995.

[27] J. Miller, A. Lazarus, B. Audoly, and P. Reis, "Shapes of a suspended curly hair," *Phys. Rev. Lett.*, vol. 112, no. 6, p. 068103, 2014.

[28] A. Lazarus, J. Miller, and P. Reis, "Continuation of equilibria and stability of slender elastic rods using an asymptotic numerical method," *J. Mech. Phys. Solids*, vol. 61, no. 8, pp. 1712–1736, 2013.

[29] A. Lazarus, J. T. Miller, M. M. Metlitz, and P. M. Reis, "Contorting a heavy and naturally curved elastic rod," *Soft Matter*, vol. 9, no. 34, pp. 8274–8281, 2013.